Journal of Volcanology and Geothermal Research 435 (2023) 107755

Contents lists available at ScienceDirect

Journal of Volcanology and Geothermal Research

journal homepage: www.journals.elsevier.com/journal-of-volcanology-and-geothermal-research

Invited Research Article

# *Re*-evaluation of the role of volatiles in the rupture of magma chambers and the triggering of crystal-rich eruptions

Catherine Annen [a,*], Virginie Pinel [b], Alain Burgisser [b]

[a] Institute of Geophysics of the Czech Academy of Sciences, Prague, Czech Republic
[b] Univ. Grenoble Alpes, Univ. Savoie Mont Blanc, CNRS, IRD, Univ. Gustave Eiffel, ISTerre, 38000 Grenoble, France

ARTICLE INFO

*Keywords:*
Magma chamber failure
Volatiles exsolution
Buoyancy
Mush eruption

ABSTRACT

The role of volatile exsolution in triggering volcanic eruption is re-evaluated using numerical simulations of a growing and solidifying magma chamber. The modelled magma chamber is silicic, emplaced at about 2 Kbar, and $H_2O$-saturated. The rate of volume additions to the chamber by the release of volatiles is controlled by cooling and solidification and is significantly lower than magma infilling rates. Thus, the increase in volume due to volatile exsolution is unlikely to be the primary cause of magma chamber failure unless the magma chamber is already on the brink of failure. However, the formation of buoyant $H_2O$ rich layers within the mush that surrounds the magma chamber makes the system gravitationally unstable. If the host rock is not permeable and volatiles accumulate, their buoyancy might overcome the strength of the wall resulting in dyke injection and possibly an eruption. Eruptions that are triggered or facilitated by volatiles exsolution are associated to the presence of mush in the chamber and are expected to be crystal-rich. Triggering of eruption by volatiles buoyancy explains the common occurrence of large ranges of crystals ages and protracted crystal residence times at low temperature.

## 1. Background

### 1.1. Introduction

Petrological data, geophysical observation, and field observation of igneous bodies and associated dykes indicate that, in many cases, magma is stored within the crust in a magma chamber before initiating its ascent to the surface and feeding an eruption. Several conditions must be fulfilled for a magma chamber located in the upper crust to feed a volcanic eruption: (1) enough melt must be present for the magma to be eruptible; (2) the magma chamber must fracture, and a dyke must initiate; (3) the dyke must be able to reach the Earth's surface without freezing first or being arrested by mechanical layering.

The final transport of magma to the surface through dyke propagation is relatively rapid, typically lasting from a few hours to a few days. This phase produces only short-term geophysical precursors (deformation or seismicity). To be able to detect and interpret longer term precursors and possibly forecast eruptions, it is essential to gain insights on the processes leading up to the rupture of magma storage zones, which marks the start of the magma final ascent (Blake and Cortés, 2018).

### 1.2. Magma chamber's rupture

Mechanical models of the processes leading to magma chamber rupture have investigated the influence of the rupture criterion considered (Albino et al., 2018; Grosfils, 2007; Gudmundsson, 2020, 2011), the local stress field (Pinel and Jaupart, 2003), a potential external trigger (Albino et al., 2010; Gottsmann et al., 2009; Pinel and Jaupart, 2005) or the rheology of the surrounding medium (Head et al., 2022; Jellinek and DePaolo, 2003). In agreement with mechanical hydrofracture models, failure is expected to be induced by tensile failure for overpressures reaching a few MPa although, in the literature, shear failure of a gravity loaded material is sometimes proposed with overpressures up to several tens of MPa (Sigmundsson et al., 2020 and references therein).

The most often evoked trigger for eruptions is an inflow of deep magma into a shallow reservoir. This process is supported by various petrological evidences such as observations of disequilibrium phenocryst assemblages or textures, inhomogeneous glass compositions, and wide ranges of glass inclusions compositions in neighboring phenocrysts (Eichelberger, 1980; Huppert et al., 1982; Samaniego et al., 2011;

* Corresponding author.
*E-mail address:* annen@ig.cas.cz (C. Annen).

https://doi.org/10.1016/j.jvolgeores.2023.107755
Received 4 May 2022; Received in revised form 13 January 2023; Accepted 18 January 2023
Available online 23 January 2023

Sparks et al., 1977). The additional volume of magma induces an increase in pressure either directly or by gas exsolution. Modelling the influence of the increase in magma volume within a storage zone on the rupture of the surrounding medium was formalized by Blake (1981) by considering that rupture occurs when the magma pressure exceeds the lithostatic pressure by an amount greater than the tensile strength of the surrounding medium and solving for the pressure evolution in a preexisting liquid-filled chamber. This model was further developed for a spherical magma chamber embedded in an infinite elastic medium by Tait et al. (1989). Following Blake (1984), Tait et al. (1989) argued that volatile exsolution resulting from the crystallization of magma by cooling was sufficient to cause chamber rupture without needing a new magma inflow.

### 1.3. Role of second boiling

The concept that eruptions are caused by the rise in pressure due to the release of a vapor phase is ancient (Morey, 1922) and remains popular (Stock et al., 2016; Tramontano et al., 2017). Phase equilibria analyses have quantified the net positive volume change induced by this so-called second boiling and the associated pressure increase, and led to the conclusion that this process can trigger eruptions from differentiated magmas stored at shallow depth (Tramontano et al., 2017). However, these analyses were performed neglecting both the compressibility of the host medium and the evolution of the magma compressibility. Importantly, they assume fast gas release and do not include the possible accommodation of the volume increase by viscous relaxation of the surrounding rocks.

### 1.4. Rheology of the country rock and pressure relaxation

The rheology of the country rock plays a decisive role in the fracturing process. In case of a perfectly elastic surrounding medium, the pressure on the chamber walls increases with each increment in magma volume, whereas in case of a viscoelastic crust, the pressure increase is released by viscous relaxation on a timescale that depends on the wallrock viscosity so that the rate of volume increase (volume per time unit) rather than the volume increase per se (volume only) is determinant in causing failure (Jellinek and DePaolo, 2003). The introduction of viscoelastic models (e.g., Huber et al., 2019; Jellinek and DePaolo, 2003; Segall, 2016) led to a departure from short-term modelling by allowing the relaxation of magma overpressure over time, this overpressure being either due to new magma inflow or to second boiling. This approach promoted a re-evaluation of the influence of magma inflow or gas release rate on the fracture behaviour of the storage zones (Caricchi et al., 2021; Edmonds and Woods, 2018) or on induced surface deformation (Townsend, 2022). The relaxation of magma overpressure also led to the consideration of another chamber rupture process that does not dissipate with time. This process is the buoyancy exerted by the accumulation of magma and volatiles at depth (Black and Manga, 2016; Caricchi et al., 2014; Malfait et al., 2014; Mittal and Richards, 2019; Sigmundsson et al., 2020).

### 1.5. Magma eruptibility

For enough melt to be present in a chamber, cooling and solidification due to heat loss through the chamber walls must be counterbalanced by regular replenishment of the chamber by new hot magma (e.g. Annen, 2009; Caricchi et al., 2014). If the melt portion relative to crystal falls below a certain threshold, the magma is locked and not eruptible. This threshold is commonly assumed to be 40–60 vol% melt, although it depends on crystal sizes and shapes as well as on the stresses applied to the suspension (Bergantz et al., 2017). Below this threshold, the crystals form a solid network and the material is a magmatic mush. Some eruptions are very crystal-rich and the magma must have been close to this lock-up threshold before erupting (e.g. Bachmann et al., 2002; Gottsmann et al., 2009). Geochronological studies of crystals in volcanic products suggest that they spent much more time at low temperature than at high temperature, which is interpreted as evidence that the erupted magma was in a mush state before being remobilized (Cooper and Kent, 2014). Several models have explored the mechanical or thermal mobilization of a mush (e.g. Burgisser and Bergantz, 2011; Carrara et al., 2020; Huber et al., 2009). They show the complex interplay between thermal convection and crystal settling (Suckale et al., 2012; Culha et al., 2020) and, in the case of mush reactivation, the emergence of a mixing bowl surrounded by static crystal-rich regions that are stilled by force chains (Bergantz et al., 2015). However, those models focus on mush fluidization and rarely address the rupture mechanics of the chamber walls needed for the onset of an eruption once the mush has been converted into eruptible magma.

### 1.6. Magma reservoirs' shape

Most mechanical models of magma chamber failure consider a preexisting storage zone, generally of simple shape (spherical), static, and in an initial state close to equilibrium. This is due to the inherent difficulty of performing mechanical modelling of the long-term evolution of a plumbing system from scratch, taking into account realistic rates of magma inflow and outflow, and the thermomechanical evolution of the surrounding environment and the magma. Real magma chambers are expected to be highly dynamic. The injection of new magma from a deeper source results in chamber growth while cooling and solidification shrink the chamber. Melting degrees vary both in space and time, and the melt-rich magma is surrounded by a mush that gradually transitions into solid rock.

In many models, magma chambers are assumed to be spherical. This simplification is useful for developing models that can be solved analytically relatively easily and can be constrained by inversion (e.g., Segall, 2013). However, if magma chambers were really starting as spheres, they would not be able to grow. Because of the inverse relationship between pressure and volume, a small spherical proto-chamber is condemned to fail and drain with any new input of magma. Magma chambers are much more likely to start as sills (Menand, 2011). New input of magma results in fracturing at the tips of the sill and in sill horizontal growth (Gudmundsson, 1990, 1986), or in vertical inflation of the sill into a laccolith (Bunger and Cruden, 2011; Gudmundsson, 1990; Menand, 2008; Pollard and Johnson, 1973; Sneddon and Mott, 1946). Field observations indicate that intrusive bodies result from the stacking of sills (e.g. de Saint Blanquat et al., 2011; Grocott et al., 2009; Gudmundsson, 1990; Michel et al., 2008; Morgan et al., 2008), while geophysical data confirm that igneous bodies are often tabular and high aspect ratio (Cruden and McCaffrey, 2001).

The largest magmatic systems on Earth are conceived as mostly continuous crystal-rich regions capped by crystal-poor regions (e.g., Bachmann, 2004; Bachmann and Bergantz, 2008). Melt reservoirs have recently been conceptualized (Cashman et al., 2017; Christopher et al., 2015; Edmonds et al., 2016; Flinders and Shen, 2017; Sparks et al., 2019) as anastomosed mush networks with a degree of interconnection that changes rapidly during awakening, possibly yielding large but transient volumes of eruptible magma (Sparks et al., 2019). A growing body of geological evidence points to mature magma storage regions characterized by mixing and hybridization occurring in an intricate plumbing system where new sills encounter both country rocks and partially or wholly crystallized storage regions generated by prior magma batches (e.g., Francalanci et al., 2005; Bouvet De Maisonneuve et al., 2013; Bachmann and Huber, 2016; Cooper, 2019; Palummo et al., 2021; Tommasini et al., 2022).

### 1.7. Modelling volatiles-bearing mush

Chamber fracturing most likely originates in the transition region between crystal-rich magma and colder country rock (Keller et al.,

2013). Recent progress has been done on characterizing the rheology of crystal mush when a gas phase is absent (e.g., Arbaret et al., 2007; Deubelbeiss et al., 2011; Cordonnier et al., 2009). Our knowledge of the rheology of gas-bearing, crystal-rich magmas, on the other hand, remains mostly superficial. Exploratory deformation experiments (e.g., Pistone et al., 2012; Pistone et al., 2015) show that the three-phase magma response to shear is complex with a combination of shear localization, crystal breakage (Forien et al., 2011), and bubble migration because of crystal rotation (Laumonier et al., 2011). When two phases are not lumped together (Suckale et al., 2016), modelling of such three-phase interactions is currently only possible within small computational volumes ($<10^2$ particles) under restricted conditions such as deformable bubbles with immobile but polyhedral crystals (e.g., Parmigiani et al., 2014; Degruyter et al., 2019) or mobile but spherical crystals (Qin and Suckale, 2017). One obstacle to progress is the struggle to find appropriate experiments to validate these seminal modelling studies (e.g., Belien et al., 2010; Furuichi and Nishiura, 2014; Oppenheimer et al., 2015). Moving away from the hot mush into colder country rock, field evidence (Spacapan et al., 2017) and laboratory measurements (Heap et al., 2020) suggest complex rheological behaviours that cannot be captured by linear elastic theory, viscoelasticity, or noncohesive granular material. Salient country rock rheological behaviours in need of rationalization are shear localization (Got et al., 2019), progressive rock damage (Holohan et al., 2017; Got et al., 2017), and plasticity changes due to thermal effects (Anderson and Segall, 2011).

In this paper, we re-evaluate the role of volatiles in triggering chamber rupture and possible eruption. We focus on the construction and long-term evolution of a plumbing system from a thermal point of view. This allows us to start the story from the beginning without introducing unrealistic initial conditions. We do not attempt to solve the complex problem of pressure evolution through time, but we rather provide quantitative information on the evolution of the volumes of melt, crystals, and gas available in the storage area. We model a magma chamber as a dynamic body that grows by addition of sills and then solidifies. We take into account the fact that the magma chamber must first be generated by the injection and accumulation of magma and that volatile release cannot be decoupled from the effect of magma injection. We consider only $H_2O$, which is the dominant volatile phase (Sobolev and Chaussidon, 1996; Wallace et al., 1995). We first test if the volume added by $H_2O$ exsolution causes magma chamber failure. We then consider exsolved $H_2O$ buoyancy as another possible mechanism of magma chamber failure.

For the sake of simplicity, we use the common semantic of magma chamber wall failure or magma chamber wall fracturing although the concept of chamber walls can be misleading because the limit between a mobile magma and the fully solid rock is more likely to be transitional with gradients in melt and crystals proportions. Thus, in this paper, the term chamber wall does not imply a sharp boundary but designate the place where a dyke can initiate and transport magma out of the molten area (Chen and Jin, 2006).

## 2. Magma chamber modelling

### 2.1. Model of magma chamber growth and solidification

We model the growth of a magma body by repeated addition of sills (Annen, 2009). Each successive sill may partially or completely crystallize depending on the time interval between injections. Unless the emplacement rate is very high, the accumulation of eruptible magma is preceded by an incubation period during which the successive sills solidify. If the magma emplacement rate is high enough to counterbalance heat loss through the country rock, a magma chamber eventually builds up (Annen, 2009). After injections stop, the magma chamber, if present, contracts as it crystallizes from the borders inwards (Annen and Burgisser, 2020).

The details of the numerical simulation, model setup, and equations are found in Annen and Burgisser (2020). We report here only the essential aspects of the model and the parameters specific to this paper. The growth of a magma body is simulated by under-accretion of 100-m thick sills that are 4, 10, and 20 km in diameter, depending on the simulation. Most results presented here are drawn from runs with sills 4 km in diameter. The first sill is emplaced at a depth of 5.5 km and the last sill is emplaced at 7.5 km. So, when sills are 4 km in diameter, the total intruded volume is 25 $km^3$. Larger sills result in volumes of magma and volatiles that increase with the square of the radius. The sills and the whole system are axisymmetric. Sills are emplaced every 100 yrs. during 2000 yrs. (1 m/yr), or every 1000 yrs. during 20,000 yrs. (0.1 m/yr), or every 10,000 yrs. during 200,000 yrs. (0.01 m/yr). After the last sill emplacement, the simulation runs until no melt remains in the system. Newly emplaced sills contain a magma at 940 °C with the composition of the monzogranite of Mt. Capanne (Elba, Italy) plus 6 wt% $H_2O$ initially dissolved in the melt (Barboni et al., 2015).

We calculate the rate of volume added by $H_2O$ exsolution during magma chamber evolution. We assume the crystallization of 10 wt% biotite. As the magma crystallizes, 0.4 wt% $H_2O$ gets locked in the biotite. The rest of the $H_2O$ concentrates in the melt. The amount of $H_2O$ in excess of saturation (6 wt%) is exsolved as an independent supercritical fluid phase. For crystal fractions <40 vol%, the bubbles of $H_2O$ are suspended in the melt. Because of their small size (Lyakhovsky et al., 1996), the buoyancy of the bubbles relative to the surrounding melt is low and they are considered immobile (Parmigiani et al., 2017). According to Parmigiani et al. (2017), connected channels of exsolved $H_2O$ form within the rigid crystal network, when exsolved $H_2O$ fraction is larger than a critical value (5–12 vol% depending on crystal fractions, Degruyter et al., 2019) and smaller than 50 vol%, and crystal fraction is in the range of 40–70 vol%. $H_2O$ is then free to move within the formed channels and rises at several centimetres per second (Parmigiani et al., 2017). Where crystal fractions exceed 70 vol%, the exsolved $H_2O$ is trapped by the crystals and cannot move further. In our simulations, we consider the rise of $H_2O$ as instantaneous, so that at each time step, the $H_2O$ moves upward from cells to cells where volatile fractions are between the critical value (recalculated at each timestep) and 50 vol%, and the crystal fractions are between 40 and 70 vol%. Everywhere else $H_2O$ is immobile. Transfer of $H_2O$ by capillary fracturing is not simulated.

Temperatures, crystal fractions, dissolved and exsolved $H_2O$ fractions are calculated on a half domain over a grid that extends vertically from the Earth's surface to a depth of 10 km and horizontally from the axis of symmetry (middle of the magma body) to a radial distance that is estimated as a function of the sill radius and the duration of the simulation to avoid boundary effects. The grid cells are 25 m × 25 m. The model parameters are reported in Table 1, the relationship between temperature and melt fraction in Fig. 1, and the model setup in Fig. 2.

**Table 1**
Value of parameters used in the numerical simulations.

| | | |
|---|---|---|
| Specific heat | 1100 | J $kg^{-1}$ |
| Latent heat | 350,000 | J $kg^{-1}$ |
| Thermal conductivity | *f(T,P)** | W $m^{-1}$ $K^{-1}$ |
| Thermal conductivity at Earth's surface | 2.25 | W $m^{-1}$ $K^{-1}$ |
| Initial geothermal gradient | 20 | °C $km^{-1}$ |
| Melt density | 2300 | kg $m^{-3}$ |
| Solid density | 2600 | kg $m^{-3}$ |
| Exsolved $H_2O$ density | *f(T,P)*** | kg $m^{-3}$ |
| Gravity acceleration | 9.81 | m $s^{-2}$ |

* Conductivities are a function of temperature and pressure as in Chapman and Furlong (1992).

** Exsolved $H_2O$ densities are a function of temperature and pressure according to the ideal gas law.

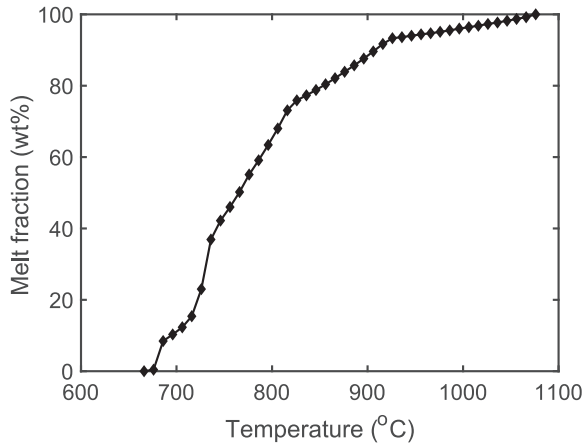


**Fig. 1.** Melt fraction-temperature relationship used in the numerical simulation. The data points were obtained with Rhyolite-MELTS (Gualda et al., 2012) for the monzogranite of Mt. Capanne (Elba, Italy) with 6 wt% $H_2O$ by Barboni et al. (2015). The values between data points are linearly interpolated.

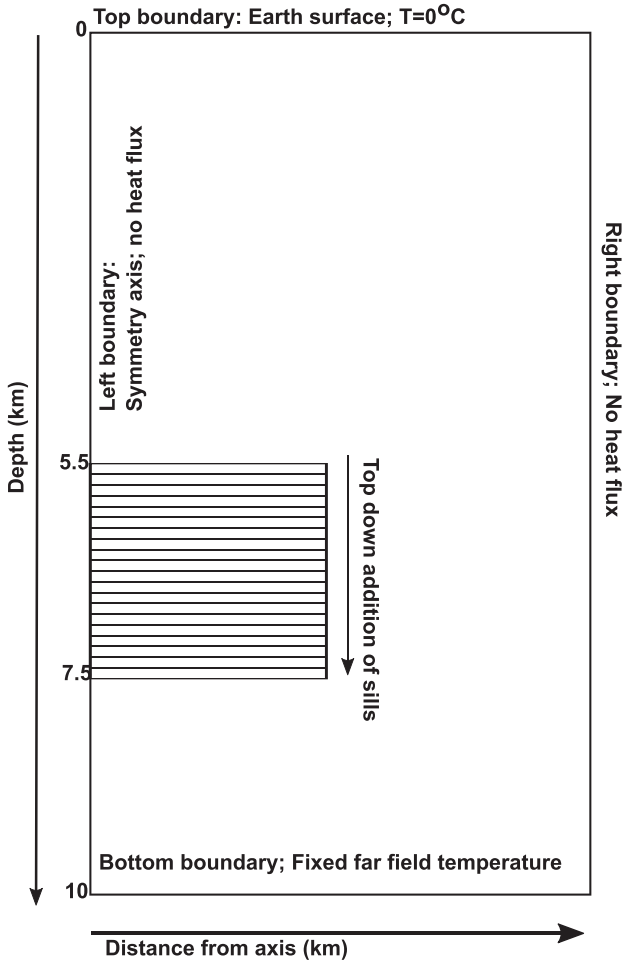


**Fig. 2.** Model setup modified from Annen and Burgisser (2020).

## 3. Pressures in a growing and solidifying magma chamber

### 3.1. Chamber overpressure due to volume increase

For non-spherical chambers with a sharp interface between magma and wallrock, the pressure depends on the shape of the chamber and on the magma and host rock compressibility (Gudmundsson, 1987; Rivalta, 2010). In our model, the chamber shape evolves as the chamber grows and solidifies (Fig. 3) and the melt fractions, volatile fractions, and temperatures vary in both space and time. The mechanical properties of our magmatic system cannot be simplified to a juxtaposition of liquid and elastoplastic solid. The rheology of the mush, the connectivity of the magma regions, and the rheology of the country rock all affect the magma pressure in complex (and understudied) ways. Calculating the pressure for a non-spherical magma chamber taking into account the gradient in rheology between the chamber and country rock, which is related to the gradient in phase proportions and temperature, is a challenging task that requires developing mechanical models able to realistically represent three-phase rheology.

For those reasons, we did not directly calculate the pressure induced by the input of magma or volatiles in the chamber. However, our thermal model allows us to calculate exsolved $H_2O$ volumes and $H_2O$ exsolution rates and to compare them with magma volumes and infilling rates. Our rationale is that, because $H_2O$ is initially transported by the magma, the added $H_2O$ volume only contributes significantly to the failing of the chamber wall if the volumetric release rate of $H_2O$ is similar to, or higher than, the magma volumetric flow rate. Otherwise, an eruption would be firstly triggered by the magma input.

### 3.2. Magma infilling rates

In the upper, brittle crust, magma chambers are likely fed by multiple episodes of dyking (Clemens and Mawer, 1992; Gudmundsson, 1990, 1986; Petford et al., 1993). Although there might be exceptions, we expect the flow of magma in a chamber to be discontinuous (Menand et al., 2015). The growth of magmatic bodies is thus characterized by at least two values of magma flow: an average flow that integrates period of repose between magma pulses, and the higher flow of individual batch injections (de Saint Blanquat et al., 2011) (Fig. 4). Regarding pressure increase inside the magma chamber, the average long-term flow is relevant only if the time interval between injection is shorter than the viscous relaxation time, $\tau$:

$$\tau = \frac{\mu}{E} \tag{1}$$

with $\mu$ and $E$ the viscosity and bulk modulus of the country rocks, respectively. The viscosity is :

$$\mu = Ae^{\frac{H}{RT}} \tag{2}$$

With the Dorn parameter $A = 10^9$ Pa s, the activation energy of creep mechanism $H = 1.3 \times 10^5$ J/mol and R, the ideal gas constant.

Viscosities and relaxation times vary exponentially with temperatures (Eqs. 1 & 2); the relaxation time is close to infinity for rocks at 100 °C, several thousand years for rocks at 300 °C, and <100 yrs. for rocks at 400 °C (Del Negro et al., 2009) (Fig. 5). For a young magma body emplaced in a cold environment, the crust behaves elastically, and the rupture of the chamber is controlled by the net volume increase due to either added magma or added $H_2O$ vapor. For a slightly more mature magma chamber embedded in a hotter environment, the crust behaves viscoelastically but its relaxation time is longer than the interval between magma injections, so that the long-term magma emplacement rate controls pressure increase. Finally, for a fully mature chamber in hot surroundings, the relaxation time is shorter than the intervals between magma injections and the short-term infilling rate of one batch of magma is controlling pressure.

The continuous volumetric flow of a single magma batch depends on the magma velocity within the feeder dyke and on the dyke dimensions. There is a minimum value for the magma flow; if the magma velocity is too low, the magma solidifies, and the dyke stops propagating. Menand et al. (2015) calculated this minimum flow to be in the range $10^{-1}$ to $10^5$ km$^3$/yr depending on the dyke dimensions, magma viscosities, and temperatures of magma and country rocks. The longer-term magma flow

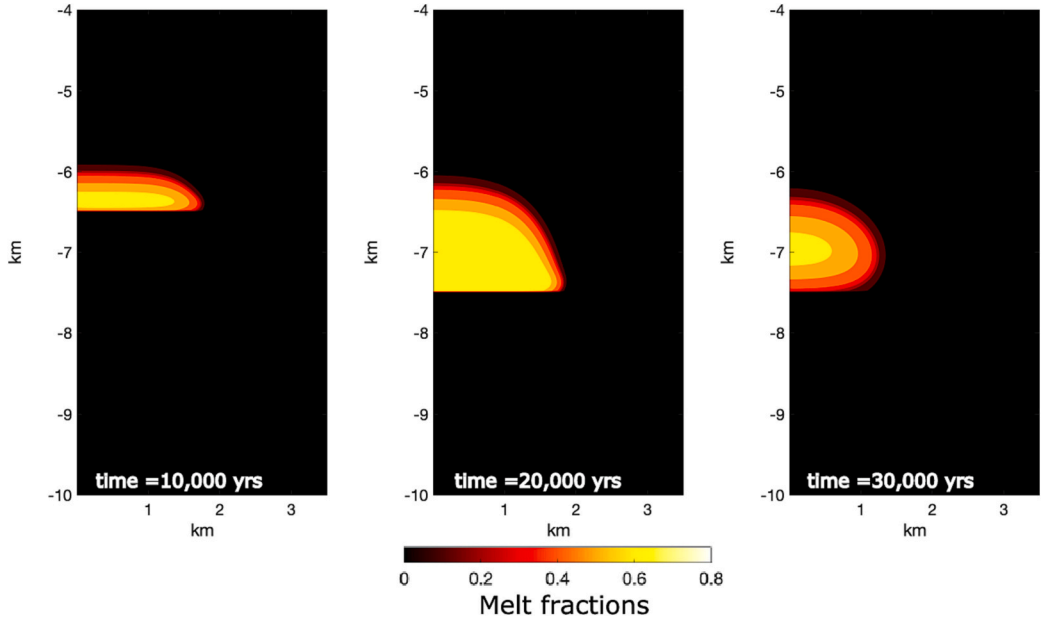


**Fig. 3.** Melt fractions in a magma body that grows at a rate of 0.1 m/y ($1.3 \times 10^{-3}$ km$^3$/yr). From left to right: (a) at time 10,000 yrs., during the growth phase; (b) at time 20,000 yrs., at the end of the growth phase; (3) at time 30,000 yrs., during the solidification phase.

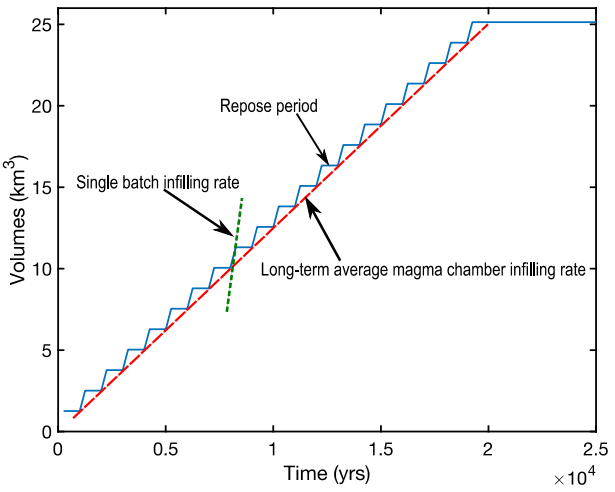


**Fig. 4.** A magma chamber grows by addition of discrete magma baches. The magma volumetric infilling rate is the slope of the volume-time relationship. The long-term average infilling rate integrates repose periods and is much lower than individual batch input rates. Figure inspired from de Saint Blanquat et al. (2011).

that integrates repose periods is significantly lower (Fig. 4). Yet, for a chamber 4 km in diameter (the smallest sill width used in this study), the formation of magma chamber requires the long-term flow to be above about $4 \times 10^{-4}$ km$^3$/yr (Annen, 2009).

To evaluate the role of $H_2O$ exsolution on the fracturing of magma chambers, we compare the volumes of exsolved $H_2O$ with the volumes of magma injected, and the $H_2O$ exsolution rates with the short-term and long-term magma infilling rates. In doing so, we neglect the compressibility of gas, melt, and surrounding country rocks, and the loss in volume due to crystallization. We will show that despite being likely overestimated, the volume increase rates due to volatiles exsolution are secondary in comparison with magma input rates.

### 3.3. Elastic host rock: Volumes of $H_2O$ exsolved relative to volumes of magma injected

$H_2O$ is exsolved and forms a new phase when $H_2O$ concentration in the residual melt exceeds saturation. Exsolved $H_2O$ is a low-density supercritical fluid that adds volume to the magma chamber. The process of $H_2O$ exsolution is progressive (Fig. 6) and controlled by solidification, hence by cooling. As long as the system is cold and the crust response to deformation is mostly elastic, the fracturing of the chamber wall is controlled by the net volumes added. The volume of added exsolved $H_2O$ does not represent more than a third of the added magma volume (Fig. 7). The addition of volume due to $H_2O$ exsolution would thus induce failure only if the chamber is already close to failure due to the input of magma. The volumes of $H_2O$ are maximum when eruptible volumes of magma are minimum and volumes of mush are maximum.

The exsolution of $H_2O$ is delayed relative to the injection of magma. At high magma chamber growth rate, the volumes of $H_2O$ reach their maximum during the solidification stage when the system is mostly composed of mush and when the country rocks are hotter and less likely to behave purely elastically. At lower emplacement rates (Figs. 6b and 7b), the volumes added by $H_2O$ relative to the injected magma volumes are maximum at an early stage, when the system is cold and mostly composed of mush. Any eruption triggered by $H_2O$ exsolution would be crystal-rich. At the lowest emplacement rates (Figs. 6c and 7c), no melt is available for an eruption.

### 3.4. Viscoelastic host rock: Rate of $H_2O$ exsolution relative to the rate of magma input

If the environment is hot enough to respond viscoelastically to pressure changes, rates of volume increase are more relevant than net volumes. If the viscosity of the surrounding rocks is still relatively high and their relaxation time is longer than the time interval between magma batches, the stress caused by successive magma injections builds up with time. To determine whether $H_2O$ exsolution plays a prominent role in starting the eruptive process, $H_2O$ exsolution rate is compared to the long-term average magma supply rate (Fig. 8). Let's first consider a magma body that grows at a rate of 0.1 m/yr by addition of sills 4 km in diameter (Fig. 8b). The long-term average magma input rate is $1.3 \times 10^{-3}$ km$^3$/yr. The highest exsolution rate for a $H_2O$-saturated magma (6

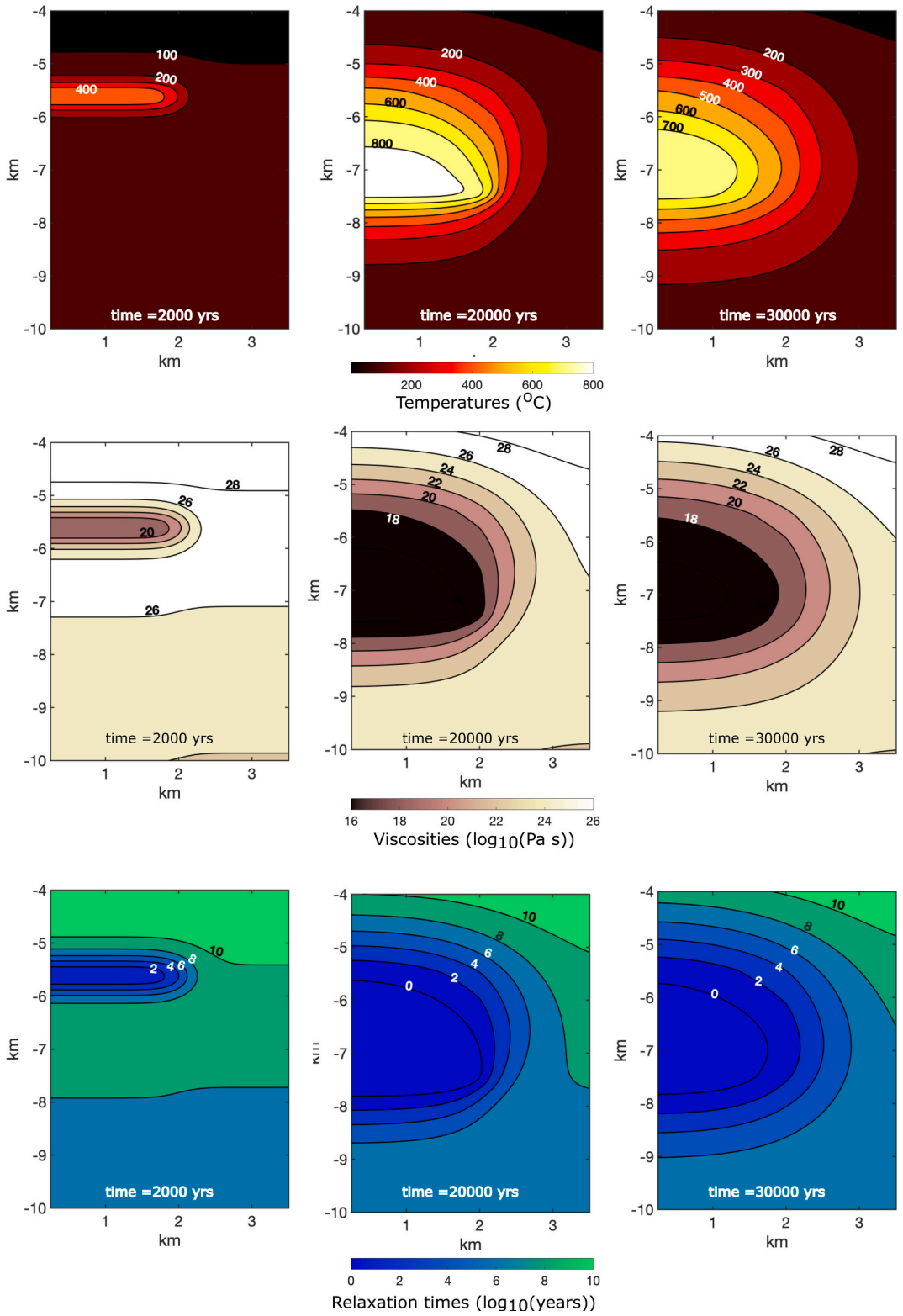


**Fig. 5.** Temperatures, country rock viscosities, and country rock relaxation times around a magma body that grows at a rate of 0.1 m/y ($1.3 \times 10^{-3}$ km$^3$/yr). From left to right: (a) at time 2000 yrs., early in the growth phase; (b) at time 20,000 yrs., at the end of the growth phase; (3) at time 30,000 yrs., during the solidification phase. Relaxation times are calculated using an elastic bulk modulus of $10^{10}$ Pa (Jellinek and DePaolo, 2003; Rubin, 1995).

wt% $H_2O$) is $5 \times 10^{-3}$ km$^3$/yr (Fig. 8b). This maximum follows the emplacement of the first sill when the country rocks are still cold and solidification is fast (Fig. 8b). The early $H_2O$ exsolution rate is higher than the long-term supply rate and contributes significantly to the added volume and resulting overpressure. The exsolution rate then rapidly decreases to a few $10^{-4}$ km$^3$/yr as the system becomes hotter. In the meantime, magma starts to accumulate and generates a magma chamber after an incubation of about 5000 yrs. At that moment, $H_2O$ exsolution rate has decreased by one order of magnitude and has become subordinate relative to magma infilling rate. For lower magma infilling rates

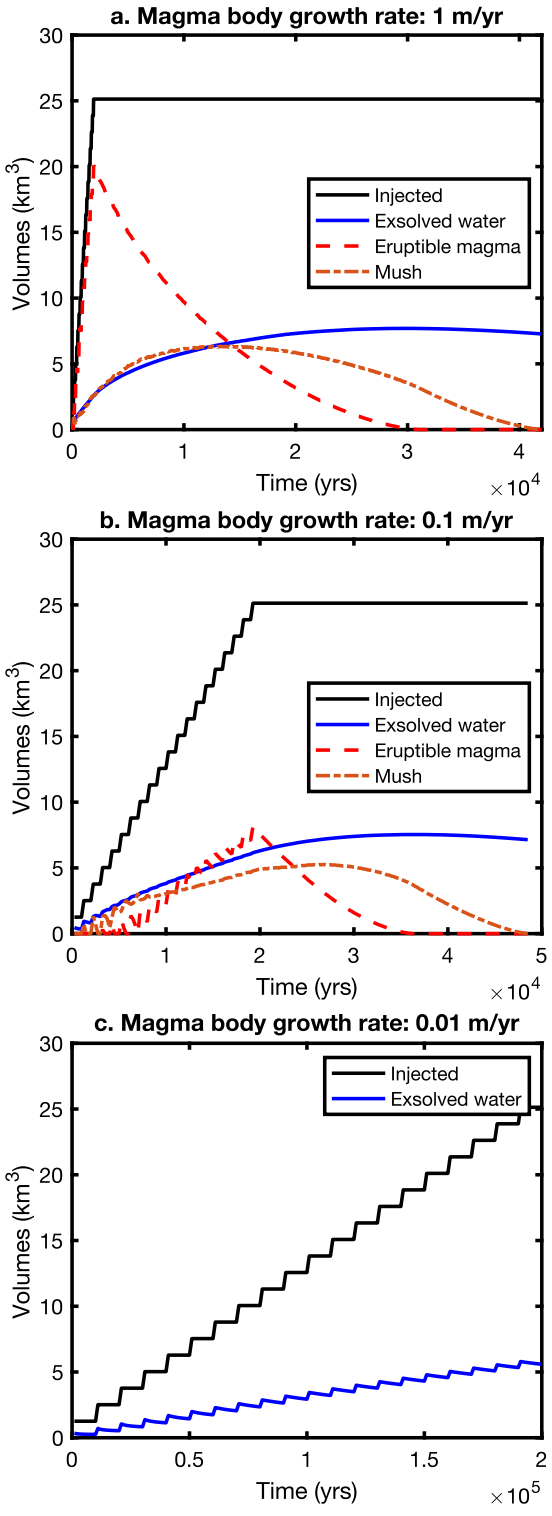


**Fig. 6.** Volumes of injected magma (water dissolved), exsolved $H_2O$, eruptible magma (> 50 wt% melt), and mush (< 50 wt% melt). The body is 4 km in diameter and grows by addition of sills until it reaches a thickness of 2 km and a volume of 25 $km^3$. Magma input then ceases, and the body solidifies. Note that the volumes of fully solidified magma are not shown. (a) Growth rates is 1 m/yr and corresponds to infilling volume rate of $1.3 \times 10^{-2}$ $km^3$/yr, (b) growth rates is 0.1 m/yr and infilling rate is $1.3 \times 10^{-3}$ $km^3$/yr, (c) growth rate is 0.01 m/yr and infilling rate is $1.3 \times 10^{-4}$ $km^3$/yr. In (c), the growth is too low for magma or mush to be present.

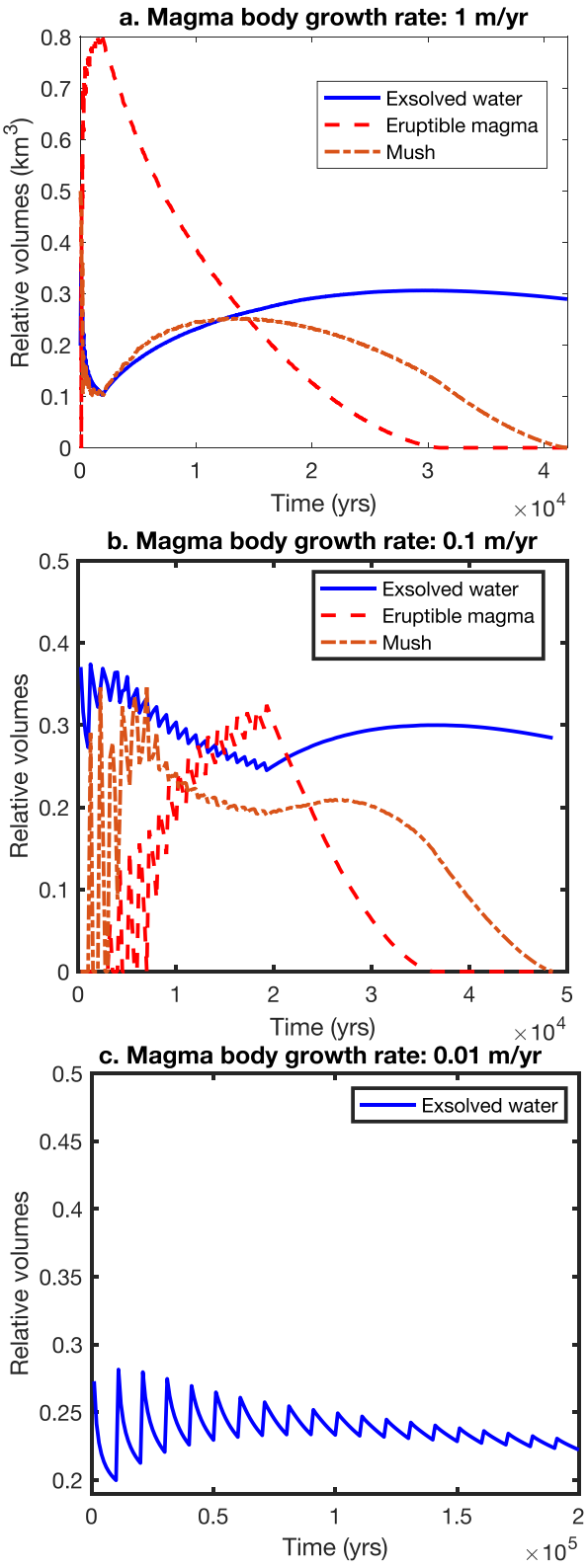


**Fig. 7.** As in Fig. 6 with volumes relative to the volumes of injected magma.

of $10^{-4}$ $km^3$/yr, the $H_2O$ exsolution rates is similar or higher than the infilling rate, but at such low magma input rate, the magma solidifies faster than it is added and no magma is available to feed an eruption (Fig. 8c). At high magma infilling rates ($10^{-2}$ $km^3$/yr, Fig. 8a), however, the $H_2O$ exsolution rate is always low relative to the infilling rate. In

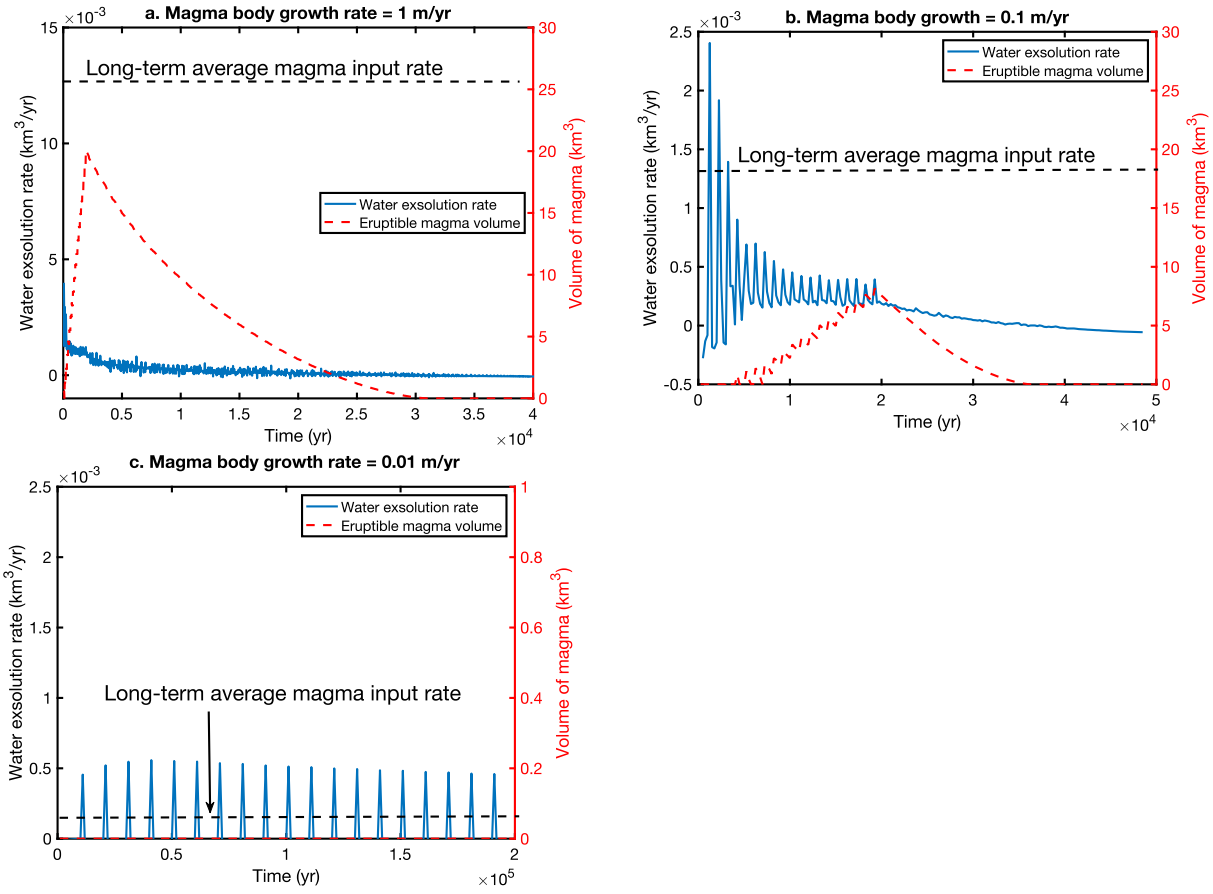


**Fig. 8.** Volume rates of $H_2O$ exsolution, and volumes of eruptible magmas. The body is 4 km in diameter. (a) Growth rates is 1 m/yr and correspond to infilling volume rate of $1.3 \times 10^{-2}$ km$^3$/yr (b) growth rates is 0.1 m/yr and infilling rate is $1.3 \times 10^{-3}$ km$^3$/yr, (c) growth rate is 0.01 m/yr and infilling rate is $1.3 \times 10^{-4}$ km$^3$/yr. In (c), the growth is too low for magma to be present.

summary, the rate of $H_2O$ exsolution adds significantly to the pressure generated by magma infilling only when the magma body is mush-dominated.

As the temperatures of the country rock increase, the relaxation times shorten and the pressure in the magma chamber may completely relax between magma batches. In this case, the $H_2O$ exsolution rate must be compared to the magma flow of an individual magma batch. The lowest volumetric flux able to sustain flow in a feeder dyke has been estimated at $10^{-1}$ km$^3$/yr (Menand et al., 2015). The rate of volume increase due to degassing is several orders of magnitude lower than the minimum volumetric flow rate of magma transported by dykes feeding the magma chamber. Thus, if the injection of one batch of magma does not cause the rupture of the chamber, the release of $H_2O$ from this magma batch does not cause rupture either. The volatile exsolution rate depends on the cooling surface of the magma body and increases with the square of the magma body radius. For the volatile exsolution rate to be comparable to the minimum flow rate of one single batch, the magma body diameter needs to be several tens of km, which corresponds to the footprint of caldera-forming magma chambers. Since the overpressure decreases with the volume of the chamber, such large magma chambers are unlikely to fail due to new volume input whether from magma injection or volatile exsolution (Jellinek and DePaolo, 2003). In addition, such an horizontally extended chamber has a high aspect ratio (sill-like) (Black and Andrews, 2020). Those magma chambers are more compressible than chambers with lower aspect ratio and less likely to fail (Rivalta, 2010).

### 3.5. Pressure due to buoyancy

Melt and exsolved $H_2O$ are less dense than the surrounding solid rocks. If the fluids are connected, their buoyancy exerts a pressure at the top of the magma body. In contrast with the pressure due to chamber volume increase, the pressure due to buoyancy is not relaxed by visco-elasticity (Black and Manga, 2016; Degruyter and Huber, 2014; Karlstrom et al., 2010). Buoyancy pressure $P$ is proportional to the height of the buoyant material $h$ and the difference in densities $\Delta\rho$ between the buoyant material and solid rocks:

$$P = \Delta\rho g h \tag{3}$$

Where $g$ is gravity. The buoyant material can be magma, magma and volatiles, or volatiles only.

Numerical simulation of $H_2O$ transfer associated to the growth and solidification of a magma chamber shows $H_2O$-rich layers forming within the mush and at the interface between mush and solid (Annen and Burgisser, 2020) (Fig. 9). In an igneous body growing by addition of sills, $H_2O$ accumulates atop each sill. If a magma chamber forms, it gets surrounded by a corona of mush, which channels the exsolved volatiles upwards (Fig. 9). As the modelled magma body solidifies, $H_2O$-rich layers get trapped in the solid roof of the chamber (Annen and Burgisser, 2020). While this result is robust from a thermal and large-scale perspective, the small-scale gas migration was not modelled. This is because the rheology of these $H_2O$-rich regions is complex.

Simulations do not allow the $H_2O$ fraction to exceed 0.5 as the material becomes volatile-supported (Parmigiani et al., 2017). In nature, if such $H_2O$ concentrations are reached, we expect a full separation of

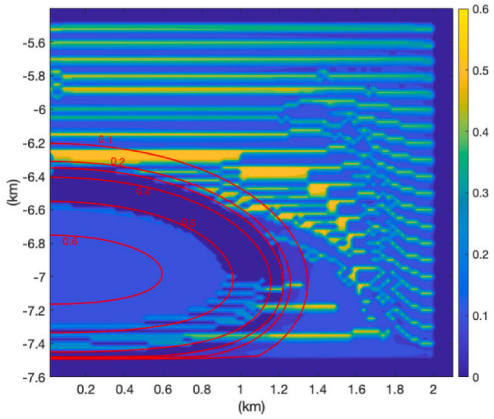


**Fig. 9.** Snapshots of the numerical simulation at 30 kyrs showing exsolved $H_2O$ volume fraction and melt fraction. Sills are 100 m thick, 2 km in radius, emplaced every 1000 years over 20 kyr. The colors show exsolved $H_2O$ volume fraction. The red contour lines show melt weight fractions. $H_2O$ accumulates at the mush-solid boundary and get trapped as crystallization proceeds. (For interpretation of the references to colour in this figure legend, the reader is referred to the web version of this article.)

crystal and $H_2O$. In this scenario, pure $H_2O$ layers will exert a buoyant pressure on the overlaying material. In the simulations, screens of $H_2O$-poor (< 0.3 vol fraction), essentially crystalline material separates $H_2O$ rich layers (0.5 vol fraction) (Fig. 9). Interstitial $H_2O$ in the crystal-rich material exerts a pressure that likely results in capillary fracturing (Pistone et al., 2015) or gas filter pressing (Holtzman et al., 2012). Temperature gradients coupled with non-linear relationships between temperatures, crystal fractions, and $H_2O$ exsolution may generate pressure gradients causing more fracturing and $H_2O$ transport between the $H_2O$-rich layers. Those processes are not modelled but are expected to connect the $H_2O$-rich layers resulting in their destabilization and aggregation (Huber et al., 2011; Oppenheimer et al., 2015).

The ability of $H_2O$ to accumulate at the top of the chamber or to, alternatively, escape from the system depends on the permeability of the mush and of the surrounding rock. To calculate the pressure the exsolved $H_2O$ exerts upwards and evaluate its role in the rupture of the magma chamber walls, we considered several hypotheses: (1) The mush is permeable and the country rock is impermeable. The exsolved $H_2O$ accumulates on top of the mush and form a single layer that is entirely decoupled from the magma body. Buoyancy pressure is controlled by the difference in densities between $H_2O$ and rocks and by the thickness of the $H_2O$ layer. (2) Both the mush and the solid country rocks are permeable enough for the $H_2O$ to escape (Black and Manga, 2017). Buoyancy is only exerted by the magma and bubbles suspended in melt. The relevant height is the height of the melt-containing body. (3) $H_2O$ remains in the mush that forms a rigid skeleton. The rising mechanism is linked to the differential pressure between $H_2O$ and solid in a poroelastic medium. This last case is treated in the next section.

The pressure exerted on the roof according to scenarios 1 and 2 are calculated with Eq. (3) and shown in Fig. 10. The overpressure needed to rupture a chamber wall in mode I (opening) and induce a dyke is close to the effective large-scale tensile strength and is estimated at a few MPa (Chen and Jin, 2006; Gudmundsson, 2011; Haimson and Rummel, 1982; Jónsson, 2012). Although this is one order of magnitude lower than the tensile strength derived in laboratory on small scale intact rock samples (Benson et al., 2012), a value of a few MPa is confirmed by estimations of overpressures leading to dyke propagation (Einarsson and Brandsdottir, 1979; Traversa et al., 2010).

When volatiles completely decouple from the magma and accumulate at the top of the magma body, the buoyancy pressure of the volatiles' layer reaches up to 9 MPa at the end of the growth phase and

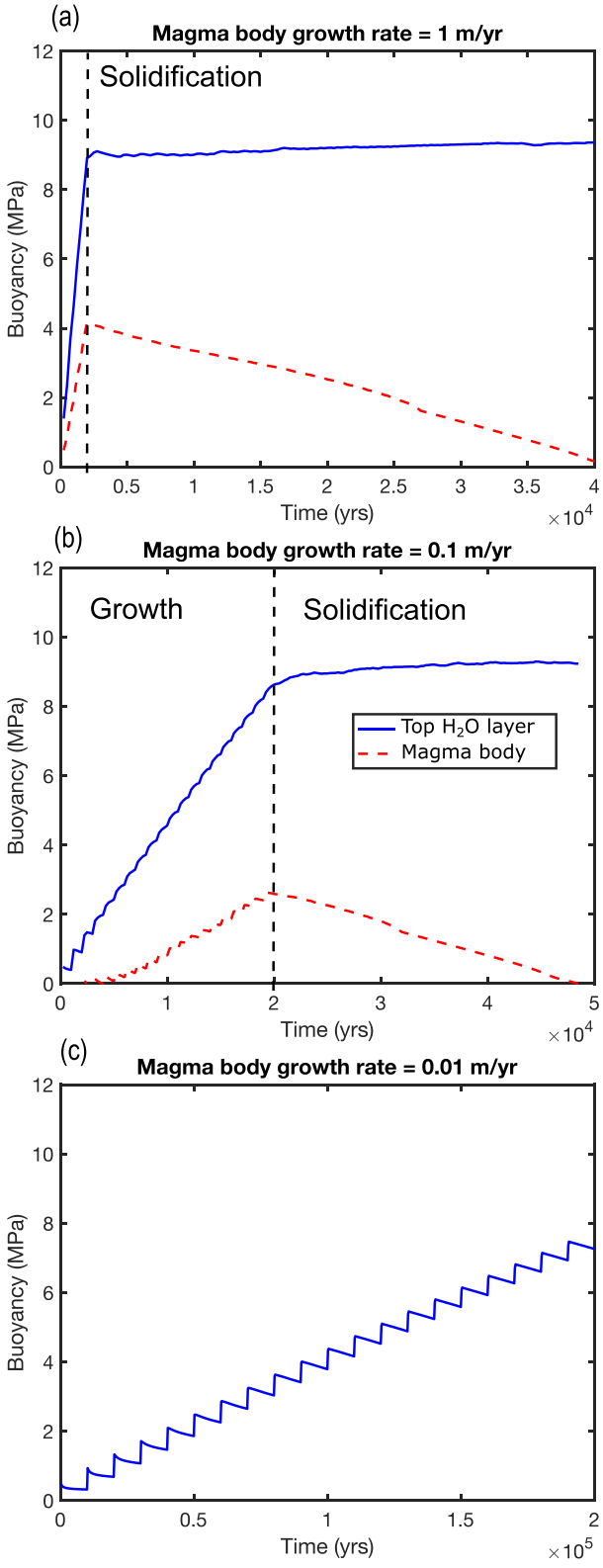


**Fig. 10.** Evolution of maximum buoyancy with time for different magma body growth rates. The solid blue curve is the buoyancy of exsolved $H_2O$ extracted from the mush and accumulated at its top. The dashed blue line is the buoyancy of the magma body assuming that exsolved volatiles have escaped from mush and solid but remain in the liquid magma as suspended bubbles. The vertical dashed line marks in (a) and (b) the end the magma body growth and the beginning of the solidification phase. In (c), the emplacement rate is too low for magma chamber to form. (For interpretation of the references to colour in this figure legend, the reader is referred to the web version of this article.)

during the solidification phase (Fig. 10), enough to cause chamber's wall rupture. During the solidification phase, $H_2O$ continues to be released by the crystalizing magma but a decrease in temperatures causes an increase in $H_2O$ density and a decrease in its volume. The two effects ($H_2O$ release and density increase) counterbalance each other. If $H_2O$ is lost through the country rock and the buoyancy is mostly exerted by the melt, the pressure increases during the magma chamber construction phase and decreases during the magma chamber solidification phase (Fig. 10). The buoyancy from the melt is always much lower than the buoyancy from the accumulated $H_2O$ because of the much lower density of $H_2O$. Buoyancy is controlled by the height of the buoyant body, whether volatile or melt. We stopped our simulations when the added intrusions reach 2 km in thickness. Adding more magma to the system would increase the height of the magma and of the $H_2O$ layer, which would make magma chamber failure due to buoyancy even more likely.

### 3.6. Effective pressure of $H_2O$ trapped in the mush

We now consider the case where the mush is not permeable enough for all $H_2O$ to be drained toward the top so that $H_2O$ remains trapped within the mush. In this case, the response of the mush $H_2O$-rich layers to stress at the macroscale level (and thus the stress they transmit to their surroundings) cannot be captured by buoyancy alone because the semirigid crystal network responds to changes occurring in interstitial $H_2O$.

If we first consider that $H_2O$ accumulates in a porous and permeable but perfectly rigid layer (i.e. neglecting poroelasticity effects), the $H_2O$ pressure will homogenize quickly due to permeable flow and the fact that the exsolved supercritical $H_2O$ is compressible. The pressure diffusion time over the distance $h$ is (Zimmerman, 2018):

$$t_p = \frac{\varphi \mu c h^2}{4k} \tag{4}$$

where $\varphi$ is the layer porosity (0.5), $\mu$ is the exsolved $H_2O$ viscosity ($1.5 \times 10^{-5}$ Pa s), $c$ is the total compressibility, which is dominated by that of the exsolved $H_2O$ ($1/150$ MPa$^{-1}$), and $k$ is the layer permeability. At an average permeability of $k = 10^{-12}$ m$^2$, $t_p = 2$ h for a layer of thickness $h = 100$ m and one month for a layer thickness h = 2 km, which is much faster than the time steps of our simulations (5 yrs).

We can now consider the effects of poroelasticity assuming that the exsolved $H_2O$ pressure follows the hydrostatic equilibrium profile of an ideal gas.

If the connected $H_2O$-rich layer can be considered isothermal, the hydrostatic equilibrium of $H_2O$ displays only small variations from top to bottom. If $P_b$ is the equilibrated exsolved $H_2O$ pressure at the layer base and $P_t$ is that atop the layer, then (see the SI for detailed calculations):

$$\frac{P_b - P_t}{P_b} = 1 - exp\left(-\frac{gM}{RT}h\right) \tag{5}$$

where $M$ is the $H_2O$ molar mass, $R$ is the gas constant, and $T$ is the temperature. At the mid-crustal conditions considered herein, the basal pressure is only 0.2% higher than the top pressure for a 100-m layer and 4% for a 2-km layer. We thus consider that the whole connected poroelastic layer will be at the same $H_2O$ pressure, $P_f$, which we define below.

The solids present in the layer have a structural rigidity that supports part of the stresses within the layer. As a result, the pressure partitions between the solids and $H_2O$ and the layer is poroelastic. The stress exerted by the layer on the surrounding country rock depends on the cohesion of the porous layer structure i.e., how the solids are connected. Loose solids, for instance, form a structure held by mutual friction. Welded grains, like crystals that underwent synneusis, have fragile bonds between each other that confers a greater rigidity to the overall structure compared to loose grains.

Cohesive effects are measured by the Biot-Wills effective stress coefficient, $\alpha$. This coefficient is a complex function of the ratio of the area occupied by $H_2O$ to the total area in a cross section in the porous material (Bear and Corapcioglu, 2012). If cohesion is nonexistent, $\alpha = 1$, whereas if solids are perfectly cohesive, $\alpha = 0$. The poroelastic approach we use is valid for small deformations, when the changes in rock damage are small enough that one value of $\alpha$ is sufficient to characterize cohesion.

To quantify the upward pressure exerted by the layer on the overlaying rocks, we need to determine $H_2O$ pressure $P_f$. We use that the $H_2O$-rich layers are mostly horizontal bodies surrounded by country rocks (Fig. 9). This geometry can be simplified to the case of a unique porous layer surrounded by rocks of homogeneous density (Fig. 11). The far-field pressure profile is the lithostatic gradient, the $H_2O$ pressure $P_f$ is constant but unknown, and the bulk pressure gradient across the layer is $\overline{P}(z) = P_t + \overline{\rho} g z$ (Keller et al., 2013). The effective pressure, $P_e$, is defined as the pressure difference between the country rock and the mechanically coupled porous layer (i.e. solid network plus interstitial $H_2O$). It can be an overpressure (positive value) or an under-pressure (negative value) depending on the vertical position. The amount of mechanical coupling is given by the coefficient α applied to $P_f$ (see SI for the full derivation):

$$P_e = \overline{P} - \alpha P_f \tag{6}$$

This situation has similarities with the initial conditions of Steam Assisted Gravity Drainage, in which steam injection at the base of an oil reservoir creates a region homogeneously saturated by steam where heat transfer, condensation, and oil drainage can then occur (Azad and Chalaturnyk, 2012). Studies of Steam Assisted Gravity Drainage suggest that the $H_2O$ pressure equilibrates close to the far-field lithostatic pressure at the level of the mid-thickness of the porous layer (Bogdanov et al., 2007). This is depicted in Fig. 11. In that case, $H_2O$ pressure exceeds lithostatic pressure at the top of the layer (and is below it at the base, respectively).

The largest $H_2O$ overpressure compared to lithostatic pressure occurs near the layer top. Considering that $P_f$ equilibrates at the mid-thickness of the porous layer, the effective pressure $P_e$ that the $H_2O$-rich layer exerts on the country rock is (see SI for details):

$$P_e = P_t(1-\alpha) - \alpha \rho_s g \frac{h}{2} \tag{7}$$

where $\rho_s$ is the solid density. Both $P_t$ and $\rho_s$ are evaluated at the layer roof; as the overlaying rocks are $H_2O$-free, $P_t$ and $\rho_g$ are set to the lithostatic values at that depth. The example of Fig. 11 shows that at most a few MPa of effective pressure can be achieved for a nearly fully connected ($\alpha = 0.98$), ~500 m thick, $H_2O$-rich layer. Lower $\alpha$ values mostly yield positive $P_e$ values that do not correspond to mode I failure. The minimum values of $\alpha$ so that $P_e \leq 0$ are given by:

$$\alpha \geq = \frac{P_t}{P_t + 0.5\rho_s g h} \tag{8}$$

Fig. 12 shows that to fracture the country rock, we need layers of $H_2O$-rich mush with low cohesivity (high α) that are several hundreds of meters thick. Such layers do not form in our simulation where volatiles fractions (and hence the parameter $\alpha$) strongly vary in space. However, our knowledge of the dynamics of volatiles and melt flow through a mush is not advanced enough to accurately model the process and determine if the conditions for effective pressure to exceed rock strength are met. Yet, the analysis suggests that, at a total pressure of 200 MPa, the effective pressure is unlikely to trigger country rock fracturing and eruption. It might play a role, though, for shallower and thicker bodies.

## 4. Discussion

### 4.1. Limitations of the models

As any model, our numerical simulations are a simplified

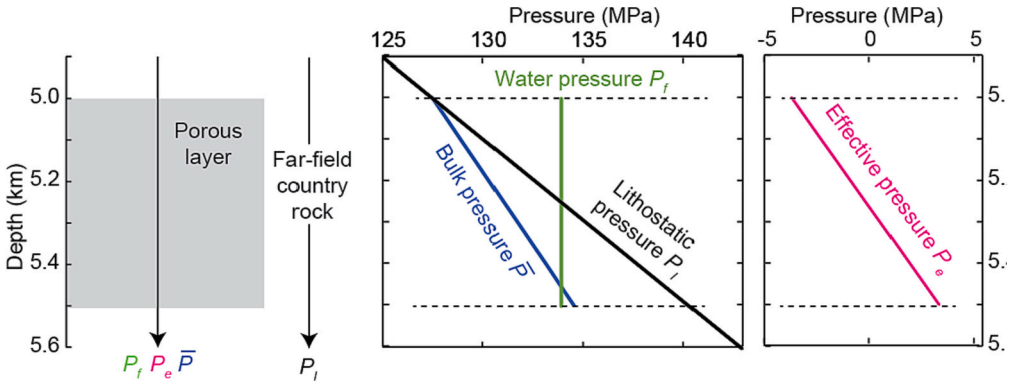


**Fig. 11.** Schematic depiction of equilibrium state of a poroelastic layer ("Porous layer") with φ =0.5, α = 0.98, $T$ = 800 °C, and solids of 2600 kg/m$^3$ embedded in a medium with a constant density of 2600 kg/m$^3$ ("Far-field country rocks"). Curves show the bulk ($\bar{P}$), lithostatic ($P_l$), $H_2O$ ($P_f$), and effective ($P_e$) pressures as a function of depth. Horizontal dashed lines indicate the roof and base of the layer, respectively. The lithostatic pressure is evaluated in the country rocks and the other pressures are evaluated across the layer.

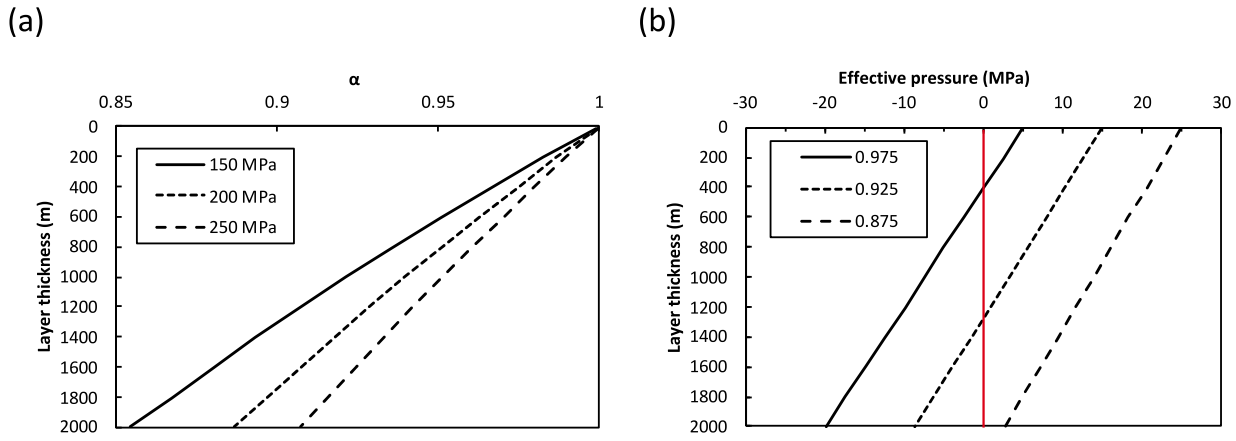


**Fig. 12.** (a) Minimum value of α for tensile forcing to occur as a function of layer thickness and for relevant values of $P_t$. (b) Effective pressure as a function of the mush layer thickness for pressure $P_t$ of 200 MPa.

representation of reality. The simplification arises from our incomplete knowledge of the processes under study and of the parameters that control them. In addition, removing some of the complexity inherent to nature is necessary to make models intelligible and useful.

In our model of magma chamber growth, the growth rate of the magma body does not change over time, and the sills that aggregate to form the body all have the same size and geometry. In nature, we expect more variations and irregularities.

Heat transfer by convection of the magma within the magma chamber or by $H_2O$ circulation in the country rock are not taken into account, possibly resulting in an underestimation of cooling rates although previous estimations suggest that this effect is minor (Annen et al., 2008).

The role of magma compressibility is neglected, which results in an overestimation of the calculated volumes that makes our results conservative. When calculating buoyancy, only upwards transfer of $H_2O$ is considered. The possible lateral draining of $H_2O$ might result in localized increased $H_2O$ height and higher pressure of buoyancy. We only consider the role of volatiles that are initially dissolved in the magma filling the chamber and we do not investigate the possible effect of volatiles exsolved in a deeper reservoir that would flux in the chamber independently of magma recharge.

We do not model the effect of volume changes due to phase transition (from melt to solid and from dissolved to exsolved $H_2O$) on deformation or flow. Our analysis of effective pressure is also very simplified as it assumes that the mush is a porous layer of homogenous porosity and temperature. Explicitly modelling complex mush processes is beyond the scope of the study presented here.

We only considered $H_2O$-saturated magma emplaced at 2 kbar, which is the pressure that is most commonly reported for upper crustal magma chambers (Huber et al., 2019). We can only speculate on the effect of other magma compositions and depths. Under-saturated magmas release less $H_2O$ and release it when more crystals are present (Annen and Burgisser, 2020), so we expect the effect of volatiles buoyancy to be less important for those magmas. Shallower magma bodies contain less $H_2O$ but also cool more rapidly in the colder host rocks. Both the effect of volatiles added volume and volatiles buoyancy might be less important. However, this could be counterbalanced by a cold crust being more prone to fracture. In contrast, deeper reservoirs can have more initial $H_2O$, but the viscosity of the surrounding crust is lower and thus this crust is less prone to fracture.

Another aspect that we do not address is the mixing of magmas of different compositions and temperatures (Salisbury et al., 2008). This could lead to a cooling and volatile exsolution that are much more rapid than modelled in this paper and that can trigger an eruption.

Future work needed to further improve our understanding of the role of volatiles in causing magma chambers failure and triggering volcanic eruptions include the development of simulations that explicitly calculate pressures and deformations and investigate different magma compositions and magma chamber depths. For more accurate models, we also need a better understanding of the physics of volatile supported fluids and of fracture propagation in the transitions of solid-mush-liquid. In the meantime, our current models still provide insights on the ability of $H_2O$ release to induce the failure of a magma chamber.

### 4.2. *The role of $H_2O$ release in triggering eruptions*

Our results indicate that the increase in magma chamber volume induced by $H_2O$ release is almost always subordinate to the increase in volume induced by magma infilling. In some cases, where the input of

magma brings the chamber on the brink of failure, volatiles exsolution could provide the additional pressure that initiates eruption. In evaluating the role of $H_2O$ in triggering eruptions, we considered pressure due to added volume and buoyancy independently, but in nature the stress on the chamber's wall is a combination of both (Sigmundsson et al., 2020). The volatiles exsolution rate is comparable to the minimum flow rate of one single intrusive event only when the magma body has the footprint of caldera-forming magma chambers. Those large magma chambers are unlikely to fail due to new volume input whether from magma injection or volatile exsolution (Jellinek and DePaolo, 2003). Thus, overall, our results support Caricchi et al. (2021) conclusion that volatile exsolution should not be as effective an eruption trigger as magma injection.

The added pressure caused by volatile exsolution is more likely to contribute to the rupture of the reservoir in the early stage of the magma chamber growth, when the system is still cold and the country rock behave elastically (Townsend et al., 2019). As noted before, at this stage, the magma body is likely to be sill-like and fracturing would occur at the sill's tip (Menand, 2008; Sneddon and Mott, 1946). The sill might extend horizontally as a result, or the magma may rise and reach the surface. We expect any eruption to be small and the resulting erupting vent to be shifted relative to the location of the magma body. One possible example is the intrusive features in the roof of the Reyðarártindur pluton, which are located at its periphery and are interpreted as eruption feeding conduits based on field and textural evidence (Rhodes et al., 2021).

If $H_2O$ separates from the mush, the pressure induced by $H_2O$ buoyancy is significant. Our simulations only partially model the separation of volatiles from the magma body, but we speculate that destabilization due to new magma input, pressure gradients due to local variations in volumes, and ductile fracturing within the mush (Weinberg and Regenauer-Lieb, 2010) can lead to discrete $H_2O$-rich layers connecting and forming larger layers at the top of the body. $SO_2$ flux measured on volcanoes confirms that volatiles can fully decouple from magma (Christopher et al., 2015; Wallace and Gerlach, 1994). Sparks et al. (2019) envisage a cascading process involving the merging of unstable melt rich layers within a mush and their increase in volume and buoyancy that promote further transport through the mush. We envisage the same cascading process for $H_2O$ rich layers that are even more buoyant and unstable than melt.

We acknowledge that the way pressures due to buoyancy are estimated in the context of magma chambers has been questioned by Gregg et al. (2015) and that more research is needed. Yet, we argue that volatiles buoyancy makes the system gravitationally unstable and either triggers eruptions or facilitates them if an additional destabilizing event occurs (e.g. new magma input, seism, fault propagation from surface) (Gottsmann et al., 2009; Gregg et al., 2012). For enough volatiles to accumulate and their overpressure to be significant, a large amount of magma must have already been emplaced so that large reservoirs are the most gravitationally unstable. It does not mean however, that a large amount of magma is available to feed an eruption since most magma may have already solidified when fracturing occurs.

We envisage three possible scenarios depending on country rock permeability and the availability of eruptible magma (Fig. 13):

Scenario 1: Volatiles are continuously lost through the country rock by capillary fracturing; no $H_2O$-rich layer forms and volatiles play no role in triggering eruptions. This scenario results in continuous surface passive degassing. If a magma chamber is present, eruptions can still be triggered by magma injections or magma buoyancy (Caricchi et al., 2014; Jellinek and DePaolo, 2003).

Scenario 2: Volatiles are drained toward the top of the mush but cannot escape through the roof. The overlaying rock eventually fractures, but either the fractures do not propagate downwards in the magma chamber or there is no eruptible magma available. Indeed, even if the igneous body grows too slowly to form a magma chamber, layers of volatiles still form at the top of the successive sills as they solidify. In this case, only the volatiles are ascending through the crust. This scenario

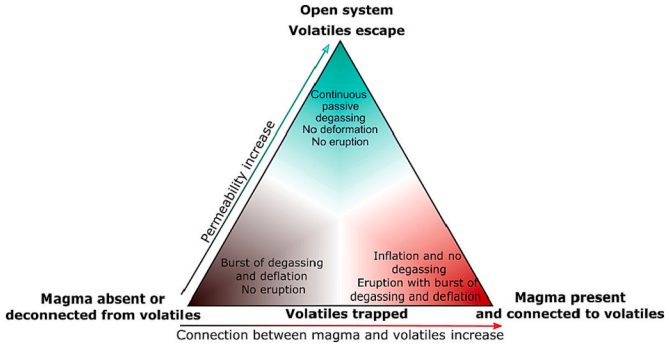


**Fig. 13.** Diagram illustrating the role of volatiles exsolved from a $H_2O$-saturated magma in the onset of eruptions and on surface manifestations.

can explain transient surface deformations (episodes of inflation followed by subsequent deflation) that are not followed by eruption. For example, unrest at Campi Flegrei (1982–1984) characterized by seismic activity and ground deformation is attributed to the massive release of magmatic gas (Bodnar et al., 2007). Burst of gas release from mature magmatic storage systems are also evoked to explain transient surface deformation in the Andes (Lundgren et al., 2020).

Scenario 3: As in scenario 2, $H_2O$-rich layers form at the chamber roof and their buoyancy either fractures the country rock or makes the system unstable and facilitates fracturing due to another agent. In this scenario, eruptible magma is present, and the failure of the magma chamber results in an eruption. The mush around the magma chamber is mobilized by the decompression induced by fracturing and volatiles ascent (Fig. 14).

### 4.3. The role of volatiles in the mobilization of mush

Eruptions driven by $H_2O$ buoyancy explain the mobilization of mush without requiring reheating by mafic magma injection (Huber et al., 2011). Because $H_2O$ is drained by the mush, the $H_2O$ height and the resulting buoyancy pressure are maximum where the amount of mush surrounding the chamber is maximum. In addition, the buoyancy of $H_2O$ layers remains high during the chamber solidification phase (Fig. 10). Further destabilization of the chamber during this period due to a new magma arrival or seismic shaking would result in a crystal-rich eruption. The mobilization of large parts of the already partially solidified body in addition to the more recently emplaced magma would account for commonly observed crystals ages spread (Fig. 14). It explains why the time crystals spend at high temperature as inferred by element diffusion profiles is short compared to radiogenic ages (Cooper and Kent, 2014). Indeed, short residence times at high temperature are expected from the crystals in the early, rapidly cooling sills that form the chamber roof. Interestingly, most of the longer U—Th crystal ages reported by Cooper and Kent (2014) are around $10^4$ yrs. This timescale fits well with our models of magma chamber growth since lower emplacement rates and longer durations do not allow for the accumulation of magma.

In our simulations, layers of volatiles are also trapped in the fully solidified upper part of the magma body (Fig. 9). This might render the plutonic part of the body easier to disaggregate and explain the incorporation in erupted products of crystals having resided for extended periods well below solidus temperatures as observed, for example, in the Central Andes (van Zalinge et al., 2022).

We expect eruptions triggered by volatiles to contain mush inclusions, but the opposite is not necessarily true i.e., mush inclusions are not necessarily the mark of a volatile-triggered eruption. According to thermal models, magma chambers are surrounded by mush independently of their volatile content so mush can also be incorporated in the magma if an eruption is triggered by new magma input or by magma buoyancy.

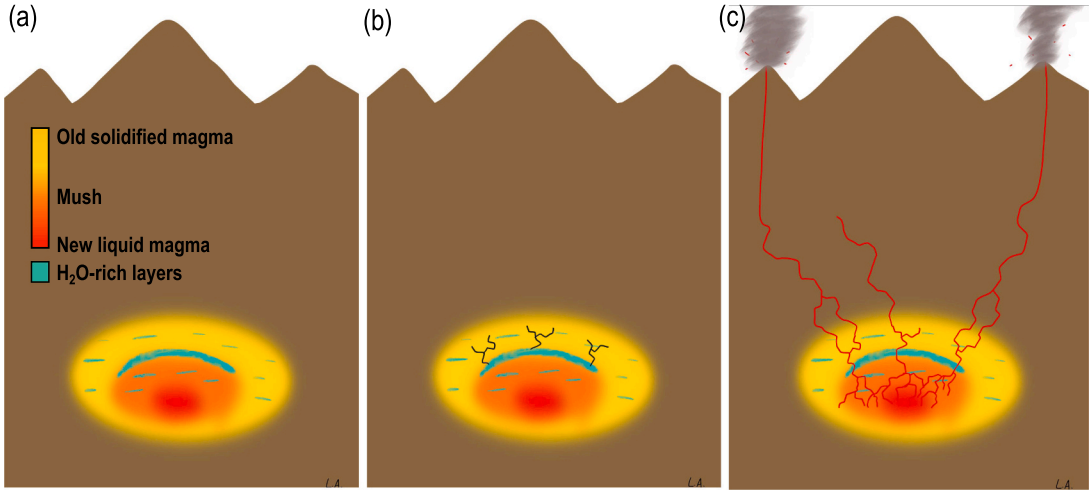


**Fig. 14.** Eruption triggered by volatiles' buoyancy. (a) Volatiles-rich layers form in the mush and get trapped in the solidified magma; (b) the buoyancy of volatiles accumulated at the top of the mush fractures the overlaying rocks; (c) fractures propagate downwards in the liquid magma chamber and upwards to the Earth's surface. The eruption incorporates magma, mush, volatiles, old and young crystals, and plutonic enclaves.

If any eruption is triggered by the added volume of $H_2O$ in a young chamber that was already over pressured by magma input, we also expect the ejecta to be crystal-rich but in this case the crystals would be young and the eruption small.

Crystal-poor and/or $H_2O$-poor eruptions like the Campanian eruption or the rhyolite eruptions of Snake River plain (Branney et al., 2007) are probably triggered by other processes than $H_2O$ buoyancy. Study of melt inclusions of the Campanian ignimbrite indicate that the magma was losing its $H_2O$ (Marianelli et al., 2006). In these cases, eruptions can be triggered by melt buoyancy or, for smaller eruptions, by new magma input.

### 4.4. *Implications for geophysical precursors*

Geophysical signals recorded several months before an eruptive event are mainly surface inflation (Bato et al., 2021; Peltier et al., 2018) and/or an increase in seismicity rate (White and McCausland, 2019). Both types of signals indicate a change in the state of stress consistent with an increase in pressure within the storage zone. Other intermediate-term precursors (Poland and Anderson, 2020) include an increase in passive degassing (e.g. Bernard et al., 2020; Carn et al., 2017; Vandemeulebrouck et al., 2000) and heat flow (Girona et al., 2021).

Probably due to the lack of joint inversion of deformation and gravity data recorded in pre-eruptive periods, there is, to our knowledge, no unambiguous observation supporting the case of an eruption triggered by second boiling without magma input. It is noteworthy that eruptions, sometimes with large volumes emitted, have occurred with unnoticed or limited precursors (e.g. Lesage et al., 2018; Sigmundsson et al., 2020). The lack of significant surface deformation and seismicity recorded before the eruption has been used as an argument in favour of second boiling as the main trigger and is generally attributed to high magma compressibility (Arzilli et al., 2019; Cassidy et al., 2019). This reasoning seems biased because if compressibility dampens the pressure increase, it will not only limit surface deformation and induced seismicity but also prevent chamber rupture. However, buoyancy of volatiles increases pressure slowly and does not immediately follow magma injection. It is therefore a good candidate to explain the absence of precursor.

In contrast, some episodic seismic bursts or inflation events are regularly recorded on non- erupting volcanoes (e.g. Biggs et al., 2014; Espín Bedón et al., 2022; Lundgren et al., 2020). These events signal a pressure increase at depth either too small to induce rupture of the surrounding medium, or not related to a significant volume of mobilizable melt. They could be interpreted as related to injection of magma in a chamber that is too solidified, too big, or embedded in a crust that is too hot (i.e. with low values of viscosity) for the trigger of an eruption (Caricchi et al., 2014; Jellinek and DePaolo, 2003). Alternatively, they could result from the sudden release of volatiles pockets disconnected from magma (Fig. 13).

One single type of precursors does not allow to discriminate between the potential causes for the unrest. However, the joint interpretation of various signals, as developed recently notably from systematic satellite observations (Reath et al., 2020, 2019), should provide clues to the processes involved in destabilizing magma storage zones. Passive degassing and deformation provide information about the permeability of the system and its evolution. Joint measurement of gravity data and deformation provide information about possible mass transfers. For example, a recent study by Gottsmann et al. (2022) using gravity and deformation data indicates that migration of fluids rather than magma is causing surface displacement above the Altiplano-Puna magma body.

## 5. Conclusions

The role of volatiles in the rupture of a magma chamber wall is linked to the thermal evolution of the magma body and the magma infilling rate. When the condition for the presence of a magma chamber is fulfilled, the volatile exsolution rate is significantly lower than the magma infilling rate. Because magma carries the volatiles and magma injection precedes volatiles exsolution, the pressure increase caused by $H_2O$ exsolution is unlikely to induce fracturing if magma injection has not done so in the first place, unless the magma chamber was brought to the brink of failure by the magma input. Young, small, and crystal-rich magma chambers are the most likely to fail due to volatile-added volume.

The formation of volatile-rich layers within the mush that surrounds the chamber makes the magma reservoir gravitationally unstable. The merging of these layers and the accumulation of volatiles at the top of the reservoir might result in enough buoyancy pressure to trigger an eruption. Buoyancy as an eruption trigger explains why some eruptions are not preceded by noticeable precursors. Because $H_2O$ is drained by the mush, $H_2O$ collection is maximum when important quantities of mush are present. In addition, as $H_2O$ accumulates with time, those eruptions are expected at a late stage in the magma body growth or during the chamber solidification. Thus, we expect eruptions driven or facilitated by volatiles buoyancy to be rich in crystals with a wide range of ages. If the magma infilling rate is too low for a magma chamber to form, $H_2O$ exsolved from the solidified magma might still form buoyant

layers and be at the origin of bradyseismic crisis.

## Data sharing

The software used to produce the results is deposited on zenodo: https://doi.org/10.5281/zenodo.6517373

## Declaration of Competing Interest

The authors declare that they have no known competing financial interests or personal relationships that could have appeared to influence the work reported in this paper.

## Data availability

All data were produced with numerical simulation. The code is available on zenodo

## Acknowledgements

CA received funding from the European Research Council (ERC) under the European Union's Horizon 2020 research and innovation programme (MAST; Grant No. 101003173). Part of the research that led to this paper was funded by the European Union's Horizon 2020 research and innovation programme under the Marie Sklodowska-Curie grant agreement No. 794594 to CA and by grant ANR-19-CE31-0007 from Agence Nationale pour la Recherche to AB. We thank Lucie Annen for drafting Fig. 14. Review by Wendy Bohrson helped us to produce an improved and better nuanced manuscript. We thank Agust Gudumdsson for his review that helped us to clarify the manuscript and for pointing us to many additional references. We thank Thierry Menand and Janine Kavanagh for their insight on sill's growth.

## Appendix A. Supplementary data

Supplementary data to this article can be found online at https://doi.org/10.1016/j.jvolgeores.2023.107755.

## References

Albino, F., Pinel, V., Sigmundsson, F., 2010. Influence of surface load variations on eruption likelihood: application to two icelandic subglacial volcanoes, Grímsvötn and Katla. Geophys. J. Int. https://doi.org/10.1111/j.1365-246X.2010.04603.x.

Albino, F., Amelung, F., Gregg, P., 2018. The role of pore fluid pressure on the failure of magma reservoirs: insights from Indonesian and Aleutian arc volcanoes. J. Geophys. Res. Solid Earth 123, 1328–1349. https://doi.org/10.1002/2017JB014523.

Anderson, K., Segall, P., 2011. Physics-based models of ground deformation and extrusion rate at effusively erupting volcanoes. J. Geophys. Res. 116 https://doi.org/10.1029/2010JB007939.

Annen, C., 2009. From plutons to magma chambers: thermal constraints on the accumulation of eruptible silicic magma in the upper crust. Earth Planet. Sci. Lett. 284, 409–416. https://doi.org/10.1016/j.epsl.2009.05.006.

Annen, C., Burgisser, A., 2020. Modeling water exsolution from a growing and solidifying felsic magma body. Lithos 105799. https://doi.org/10.1016/j.lithos.2020.105799.

Annen, C., Pichavant, M., Bachmann, O., Burgisser, A., 2008. Conditions for the growth of a long-lived shallow crustal magma chamber below Mount Pelee volcano (Martinique, Lesser Antilles Arc). J. Geophys. Res. 113 https://doi.org/10.1029/2007JB005049.

Arbaret, L., Bystricky, M., Champallier, R., 2007. Microstructures and rheology of hydrous synthetic magmatic suspensions deformed in torsion at high pressure. J. Geophys. Res. 112 https://doi.org/10.1029/2006JB004856.

Arzilli, F., Morgavi, D., Petrelli, M., Polacci, M., Burton, M., Di Genova, D., Spina, L., La Spina, G., Hartley, M.E., Romero, J.E., Fellowes, J., Diaz-Alvarado, J., Perugini, D., 2019. The unexpected explosive sub-Plinian eruption of Calbuco volcano (22–23 April 2015; southern Chile): triggering mechanism implications. J. Volcanol. Geotherm. Res. 378, 35–50. https://doi.org/10.1016/j.jvolgeores.2019.04.006.

Azad, A., Chalaturnyk, R.J., 2012. An improved SAGD analytical simulator: Circular steam chamber geometry. J. Pet. Sci. Eng. 82–83, 27–37. https://doi.org/10.1016/j.petrol.2012.01.003.

Bachmann, O., 2004. On the Origin of Crystal-poor Rhyolites: Extracted from Batholithic Crystal Mushes. J. Petrol. 45, 1565–1582. https://doi.org/10.1093/petrology/egh019.

Bachmann, O., Bergantz, G.W., 2008. Rhyolites and their Source Mushes across Tectonic Settings. J. Petrol. 49, 2277–2285. https://doi.org/10.1093/petrology/egn068.

Bachmann, O., Huber, C., 2016. Silicic magma reservoirs in the Earth's crust. Am. Mineral. 101, 2377–2404. https://doi.org/10.2138/am-2016-5675.

Bachmann, O., Dungan, M.A., Lipman, P.W., 2002. The Fish Canyon magma body, San Juan volcanic field, Colorado: Rejuvenation and eruption of an upper-crustal batholith. J. Petrol. 43, 1469–1503.

Barboni, M., Annen, C., Schoene, B., 2015. Evaluating the construction and evolution of upper crustal magma reservoirs with coupled U/Pb zircon geochronology and thermal modeling: a case study from the Mt. Capanne pluton (Elba, Italy). Earth Planet. Sci. Lett. 432, 436–448. https://doi.org/10.1016/j.epsl.2015.09.043.

Bato, M.G., Lundgren, P., Pinel, V., Solidum, R., Daag, A., Cahulogan, M., 2021. The 2020 Eruption and large Lateral Dike Emplacement at Taal Volcano, Philippines: Insights from Satellite Radar Data. Geophys. Res. Lett. 48, e2021GL092803 https://doi.org/10.1029/2021GL092803.

Bear, J., Corapcioglu, M.Y., 2012. Transport Processes in Porous Media. Springer Science & Business Media.

Belien, I.B., Cashman, K.V., Rempel, A.W., 2010. Gas accumulation in particle-rich suspensions and implications for bubble populations in crystal-rich magma. Earth Planet. Sci. Lett. 297, 133–140. https://doi.org/10.1016/j.epsl.2010.06.014.

Benson, P.M., Heap, M.J., Lavallée, Y., Flaws, A., Hess, K.-U., Selvadurai, A.P.S., Dingwell, D.B., Schillinger, B., 2012. Laboratory simulations of tensile fracture development in a volcanic conduit via cyclic magma pressurisation. Earth Planet. Sci. Lett. 349–350, 231–239. https://doi.org/10.1016/j.epsl.2012.07.003.

Bergantz, G.W., Schleicher, J.M., Burgisser, A., 2015. Open-system dynamics and mixing in magma mushes. Nat. Geosci. 8, 793–796. https://doi.org/10.1038/ngeo2534.

Bergantz, G.W., Schleicher, J.M., Burgisser, A., 2017. On the kinematics and dynamics of crystal-rich systems. J. Geophys. Res. Solid Earth 122, 6131–6159. https://doi.org/10.1002/2017JB014218.

Bernard, A., Villacorte, E., Maussen, K., Caudron, C., Robic, J., Maximo, R., Rebadulla, R., Bornas, M., Solidum, R., 2020. Carbon dioxide in Taal volcanic lake: a simple gasometer for volcano monitoring. Geophys. Res. Lett. https://doi.org/10.1029/2020GL090884.

Biggs, J., Ebmeier, S.K., Aspinall, W.P., Lu, Z., Pritchard, M.E., Sparks, R.S.J., Mather, T. A., 2014. Global link between deformation and volcanic eruption quantified by satellite imagery. Nat. Commun. 5, 3471. https://doi.org/10.1038/ncomms4471.

Black, B.A., Andrews, B.J., 2020. Petrologic imaging of the architecture of magma reservoirs feeding caldera-forming eruptions. Earth Planet. Sci. Lett. 552, 116572 https://doi.org/10.1016/j.epsl.2020.116572.

Black, B.A., Manga, M., 2016. The eruptibility of magmas at Tharsis and Syrtis Major on Mars. J. Geophys. Res. Planets 121, 944–964. https://doi.org/10.1002/2016JE004998.

Black, B.A., Manga, M., 2017. Volatiles and the tempo of flood basalt magmatism. Earth Planet. Sci. Lett. 458, 130–140. https://doi.org/10.1016/j.epsl.2016.09.035.

Blake, S., 1981. Volcanism and the dynamics of open magma chamber. Nature 289, 783–785.

Blake, S., 1984. Magma mixing and hybridization processes at the alkalic, silicic, Torfajökull Central Volcano triggered by tholeiitic Veidivötn fissuring, South Iceland. J. Volcanol. Geotherm. Res. 22, 1–31.

Blake, S., Cortés, J.A., 2018. Forecasting deflation, intrusion and eruption at inflating volcanoes. Earth Planet. Sci. Lett. 481, 246–254. https://doi.org/10.1016/j.epsl.2017.10.040.

Bodnar, R.J., Cannatelli, C., De Vivo, B., Lima, A., Belkin, H.E., Milia, A., 2007. Quantitative model for magma degassing and ground deformation (bradyseism) at Campi Flegrei, Italy: Implications for future eruptions. Geol 35, 791. https://doi.org/10.1130/G23653A.1.

Bogdanov, I., El Ganaoui, M., Kamp, A., 2007. COMSOL 2D Simulation of Heavy Oil Recovery by Steam Assisted Gravity Drainage.

Bouvet De Maisonneuve, C., Dungan, M.A., Bachmann, O., Burgisser, A., 2013. Petrological Insights into Shifts in Eruptive Styles at Volcan Llaima (Chile). J. Petrol. 54, 393–420. https://doi.org/10.1093/petrology/egs073.

Branney, M.J., Bonnichsen, B., Andrews, G.D.M., Ellis, B., Barry, T.L., McCurry, M., 2007. "Snake River (SR)-type" volcanism at Yellowstone hotspot track: distintive products from unusual, high temperature silicic super-eruptions. Bull. Volcanol. https://doi.org/10.1007/s00445-007-0140-7.

Bunger, A.P., Cruden, A.R., 2011. Modeling the growth of laccoliths and large mafic sills: Role of magma body forces. J. Geophys. Res. Solid Earth 116. https://doi.org/10.1029/2010jb007648.

Burgisser, A., Bergantz, G.W., 2011. A rapid mechanism to remobilize and homogenize highly crystalline magma bodies. Nature 471, 212–U97. https://doi.org/10.1038/nature09799.

Caricchi, L., Annen, C., Blundy, J., Simpson, G., Pinel, V., 2014. Frequency and magnitude of volcanic eruptions controlled by magma injection and buoyancy. Nat. Geosci. 7, 126–130. https://doi.org/10.1038/ngeo2041.

Caricchi, L., Townsend, M., Rivalta, E., Namiki, A., 2021. The build-up and triggers of volcanic eruptions. Nat. Rev. Earth Environ. 2, 458–476. https://doi.org/10.1038/s43017-021-00174-8.

Carn, S.A., Fioletov, V.E., McLinden, C.A., Li, C., Krotkov, N.A., 2017. A decade of global volcanic SO2 emissions measured from space. Sci. Rep. 7, 44095. https://doi.org/10.1038/srep44095.

Carrara, A., Burgisser, A., Bergantz, G., 2020. The Architecture of Intrusions in Magmatic Mush. https://doi.org/10.1016/j.epsl.2020.116539.

Cashman, K.V., Sparks, R.S.J., Blundy, J.D., 2017. Vertically extensive and unstable magmatic systems: a unified view of igneous processes. Science 355. https://doi.org/10.1126/science.aag3055.

Cassidy, M., Ebmeier, S.K., Helo, C., Watt, S.F.L., Caudron, C., Odell, A., Spaans, K., Kristianto, P., Triastuty, H., Gunawan, H., Castro, J.M., 2019. Explosive Eruptions with Little Warning: Experimental Petrology and Volcano monitoring Observations

from the 2014 Eruption of Kelud, Indonesia. Geochem. Geophys. Geosyst. 20, 4218–4247. https://doi.org/10.1029/2018GC008161.
Chapman, D.S., Furlong, K.P., 1992. Thermal state of the continental lower crust. In: Fountain, D.M., Arculus, R., Kay, R.W. (Eds.), Continental Lower Crust, Developments in Geotectonics, 23. Elsevier, pp. 179–199.
Chen, Z., Jin, Z.-H., 2006. Magma-driven subcritical crack growth and implications for dike initiation from a magma chamber. Geophys. Res. Lett. 33 https://doi.org/10.1029/2006GL026979.
Christopher, T.E., Blundy, J., Cashman, K., Cole, P., Edmonds, M., Smith, P.J., Sparks, R. S.J., Stinton, A., 2015. Crustal-scale degassing due to magma system destabilization and magma-gas decoupling at Soufrière Hills Volcano, Montserrat. Geochem. Geophys. Geosyst. 16, 2797–2811. https://doi.org/10.1002/2015GC005791.
Clemens, J.D., Mawer, C.K., 1992. Granitic Magma Transport by Fracture Propagation. Tectonophysics 204, 339–360.
Cooper, K.M., 2019. Time scales and temperatures of crystal storage in magma reservoirs: implications for magma reservoir dynamics. Philos. Trans. R. Soc. A Math. Phys. Eng. Sci. 377, 20180009. https://doi.org/10.1098/rsta.2018.0009.
Cooper, K.M., Kent, A.J.R., 2014. Rapid remobilization of magmatic crystals kept in cold storage. Nature 506, 480–483. https://doi.org/10.1038/nature13280.
Cordonnier, B., Hess, K.-U., Lavallee, Y., Dingwell, D.B., 2009. Rheological properties of dome lavas: Case study of Unzen volcano. Earth Planet. Sci. Lett. 279, 263–272. https://doi.org/10.1016/j.epsl.2009.01.014.
Cruden, A.R., McCaffrey, K.J.W., 2001. Growth of plutons by floor subsidence: Implications for rates of emplacement, intrusion spacing and melt-extraction mechanisms. Phys. Chem. Earth Pt. A-Solid Earth Geod. 26, 303–315.
Culha, C., Suckale, J., Keller, T., Qin, Z., 2020. Crystal fractionation by crystal-driven convection. Geophys. Res. Lett. 47, e2019GL086784 https://doi.org/10.1029/2019GL086784.
de Saint Blanquat, M., Horsman, E., Habert, G., Morgan, S., Vanderhaeghe, O., Law, R., Tikoff, B., 2011. Multiscale magmatic cyclicity, duration of pluton construction, and the paradoxical relationship between tectonism and plutonism in continental arcs. Tectonophysics 500, 20–33.
Degruyter, W., Huber, C., 2014. A model for eruption frequency of upper crustal silicic magma chambers. Earth Planet. Sci. Lett. 403, 117–130. https://doi.org/10.1016/j.epsl.2014.06.047.
Degruyter, W., Parmigiani, A., Huber, C., Bachmann, O., 2019. How do volatiles escape their shallow magmatic hearth? Philos. Trans. R. Soc. Lond. A 377, 20180017. https://doi.org/10.1098/rsta.2018.0017.
Del Negro, C., Currenti, G., Scandura, D., 2009. Temperature-dependent viscoelastic modeling of ground deformation: Application to Etna volcano during the 1993–1997 inflation period. Phys. Earth Planet. Inter. 172, 299–309. https://doi.org/10.1016/j.pepi.2008.10.019.
Deubelbeiss, Y., Kaus, B.J.P., Connolly, J.A.D., Caricchi, L., 2011. Potential causes for the non-Newtonian rheology of crystal-bearing magmas. Geochem. Geophys. Geosyst. 12.
Edmonds, M., Woods, A.W., 2018. Exsolved volatiles in magma reservoirs. J. Volcanol. Geotherm. Res. 368, 13–30. https://doi.org/10.1016/j.jvolgeores.2018.10.018.
Edmonds, M., Kohn, S.C., Hauri, E.H., Humphreys, M.C.S., Cassidy, M., 2016. Extensive, water-rich magma reservoir beneath southern Montserrat. Lithos 252–253, 216–233. https://doi.org/10.1016/j.lithos.2016.02.026.
Eichelberger, J.C., 1980. Vesiculation of mafic magma during replenishment of silicic magma reservoirs. Nature 288, 446–450.
Einarsson, P., Brandsdottir, B., 1979. Seismological evidence for lateral magma intrusion during the 1978 deflation of the Krafla Volcano in NE Iceland. J. Geophys. 47, 160–165.
Espín Bedón, P.A., Audin, L., Doin, M.-P., Pinel, V., Pathier, E., Mothes, P., García, A., Samaniego, P., Pacheco, D., 2022. Unrest at Cayambe Volcano revealed by SAR imagery and seismic activity after the Pedernales subduction earthquake, Ecuador (2016). J. Volcanol. Geotherm. Res. 428, 107577 https://doi.org/10.1016/j.jvolgeores.2022.107577.
Flinders, A.F., Shen, Y., 2017. Seismic evidence for a possible deep crustal hot zone beneath Southwest Washington. Sci. Rep. 7, 7400. https://doi.org/10.1038/s41598-017-07123-w.
Forien, M., Arbaret, L., Burgisser, A., Champallier, R., 2011. Experimental constrains on shear-induced crystal breakage in magmas. J. Geophys. Res. 116 https://doi.org/10.1029/2010JB008026.
Francalanci, L., Davies, G.R., Lustenhouwer, W., Tommasini, S., Mason, P.R.D., Conticelli, S., 2005. Intra-grain Sr isotope evidence for crystal recycling and multiple magma reservoirs in the recent activity of stromboli Volcano, Southern Italy. J. Pet. 46, 1997–2021. https://doi.org/10.1093/petrology/egi045.
Furuichi, M., Nishiura, D., 2014. Robust coupled fluid-particle simulation scheme in Stokes-flow regime: toward the geodynamic simulation including granular media. Geochem. Geophys. Geosyst. 15, 2865–2882. https://doi.org/10.1002/2014GC005281.
Girona, T., Realmuto, V., Lundgren, P., 2021. Large-scale thermal unrest of volcanoes for years prior to eruption. Nat. Geosci. 14, 238–241. https://doi.org/10.1038/s41561-021-00705-4.
Got, J.-L., Carrier, A., Marsan, D., Jouanne, F., Vogfjörd, K., Villemin, T., 2017. An analysis of the nonlinear magma-edifice coupling at Grimsvötn volcano (Iceland). J. Geophys. Res. Solid Earth 122, 2016JB012905. https://doi.org/10.1002/2016JB012905.
Got, J.-L., Amitrano, D., Stefanou, I., Brothelande, E., Peltier, A., 2019. Damage and strain localization around a pressurized shallow-level magma reservoir. J. Geophys. Res. Solid Earth 124, 1443–1458. https://doi.org/10.1029/2018JB016407.
Gottsmann, J., Lavallée, Y., Martí, J., Aguirre-Díaz, G., 2009. Magma–tectonic interaction and the eruption of silicic batholiths. Earth Planet. Sci. Lett. 284, 426–434. https://doi.org/10.1016/j.epsl.2009.05.008.
Gottsmann, J., Eiden, E., Pritchard, M.E., 2022. Transcrustal compressible fluid flow explains the Altiplano-Puna gravity and deformation anomalies. Geophys. Res. Lett. 49, e2022GL099487 https://doi.org/10.1029/2022GL099487.
Gregg, P.M., de Silva, S.L., Grosfils, E.B., Parmigiani, J.P., 2012. Catastrophic caldera-forming eruptions: Thermomechanics and implications for eruption triggering and maximum caldera dimensions on Earth. J. Volcanol. Geotherm. Res. 241–242, 1–12. https://doi.org/10.1016/j.jvolgeores.2012.06.009.
Gregg, P.M., Grosfils, E.B., de Silva, S.L., 2015. Catastrophic caldera-forming eruptions II: the subordinate role of magma buoyancy as an eruption trigger. J. Volcanol. Geotherm. Res. 305, 100–113. https://doi.org/10.1016/j.jvolgeores.2015.09.022.
Grocott, J., Arevalo, C., Welkner, D., Cruden, A., 2009. Fault-assisted vertical pluton growth: Coastal Cordillera, north Chilean Andes. J. Geol. Soc. 166, 295–301.
Grosfils, E.B., 2007. Magma reservoir failure on the terrestrial planets: Assessing the importance of gravitational loading in simple elastic models. J. Volcanol. Geotherm. Res. 166, 47–75. https://doi.org/10.1016/j.jvolgeores.2007.06.007.
Gualda, G.A.R., Ghiorso, M.S., Lemons, R.V., Carley, T.L., 2012. Rhyolite-MELTS: a modified calibration of MELTS optimized for silica-rich, fluid-bearing magmatic systems. J. Petrol. 53, 875–890. https://doi.org/10.1093/petrology/egr080.
Gudmundsson, Å., 1986. Formation of crystal magma chambers in Iceland. Geology 14, 164–166. https://doi.org/10.1130/0091-7613(1986)14<164:FOCMCI>2.0.CO;2.
Gudmundsson, A., 1987. Lateral magma flow, caldera collapse, and a mechanism of large eruption in Iceland. J. Volcanol. Geotherm. Res. 34, 65–78.
Gudmundsson, A., 1990. Emplacement of dikes, sills and crustal magma chambers ar divergent plate boundaries. Tectonophysics 176, 257–275.
Gudmundsson, A., 2011. Rock Fractures in Geological Processes. Cambridge University Press.
Gudmundsson, A., 2020. Volcanotectonics: Understanding the Structure, Deformation and Dynamics of Volcanoes. Cambridge University Press.
Haimson, B.C., Rummel, F., 1982. Hydrofracturing stress measurements in the Iceland Research Drilling Project drill hole at Reydarfjordur, Iceland. J. Geophys. Res. 87, 6631–6649. https://doi.org/10.1029/JB087iB08p06631.
Head, M., Hickey, J., Thompson, J., Gottsmann, J., Fournier, N., 2022. Rheological controls on magma reservoir failure in a thermo-viscoelastic crust. J. Geophys. Res. Solid Earth 127, e2021JB023439. https://doi.org/10.1029/2021JB023439.
Heap, M.J., Villeneuve, M., Albino, F., Farquharson, J.I., Brothelande, E., Amelung, F., Got, J.-L., Baud, P., 2020. Towards more realistic values of elastic moduli for volcano modelling. J. Volcanol. Geotherm. Res. 390, 106684 https://doi.org/10.1016/j.jvolgeores.2019.106684.
Holohan, E.P., Sudhaus, H., Walter, T.R., Schöpfer, M.P.J., Walsh, J.J., 2017. Effects of Host-rock Fracturing on Elastic-deformation Source Models of Volcano Deflation. Sci. Rep. 7, 10970. https://doi.org/10.1038/s41598-017-10009-6.
Holtzman, R., Szulczewski, M.L., Juanes, R., 2012. Capillary Fracturing in Granular Media. Phys. Rev. Lett. 108, 264504 https://doi.org/10.1103/PhysRevLett.108.264504.
Huber, C., Bachmann, O., Manga, M., 2009. Homogenization processes in silicic magma chambers by stirring and mushification (latent heat buffering). Earth Planet. Sci. Lett. 283, 38–47. https://doi.org/10.1016/j.epsl.2009.03.029.
Huber, C., Bachmann, O., Dufek, J., 2011. Thermo-mechanical reactivation of locked crystal mushes: Melting-induced internal fracturing and assimilation processes in magmas. Earth Planet. Sci. Lett. 304, 443–454.
Huber, C., Townsend, M., Degruyter, W., Bachmann, O., 2019. Optimal depth of subvolcanic magma chamber growth controlled by volatiles and crust rheology. Nat. Geosci. 12, 762–768. https://doi.org/10.1038/s41561-019-0415-6.
Huppert, H.E., Sparks, R.S.J., Turner, J.S., 1982. Effects of volatiles on mixing in calc-alkaline magma systems. Nature 297, 554–557. https://doi.org/10.1038/297554a0.
Jellinek, A.M., DePaolo, D.J., 2003. A model for the origin of large silicic magma chambers: precursors of caldera-forming eruptions. Bull. Volcanol. 65, 363–381.
Jónsson, S., 2012. Tensile rock mass strength estimated using InSAR. Geophys. Res. Lett. 39 https://doi.org/10.1029/2012GL053309.
Karlstrom, L., Dufek, J., Manga, M., 2010. Magma chamber stability in arc and continental crust. J. Volcanol. Geotherm. Res. 190, 249–270. https://doi.org/10.1016/j.jvolgeores.2009.10.003.
Keller, T., May, D.A., Kaus, B.J.P., 2013. Numerical modelling of magma dynamics coupled to tectonic deformation of lithosphere and crust. Geophys. J. Int. 195, 1406–1442. https://doi.org/10.1093/gji/ggt306.
Laumonier, M., Arbaret, L., Burgisser, A., Champallier, R., 2011. Porosity redistribution enhanced by strain localization in crystal-rich magmas. Geology 39, 715–718. https://doi.org/10.1130/G31803.1.
Lesage, P., Carrara, A., Pinel, V., Arámbula-Mendoza, R., 2018. Absence of Detectable Precursory Deformation and Velocity Variation before the large Dome Collapse of July 2015 at Volcán de Colima, Mexico. Front. Earth Sci. 6.
Lundgren, P., Girona, T., Bato, M.G., Realmuto, V.J., Samsonov, S., Cardona, C., Franco, L., Gurrola, E., Aivazis, M., 2020. The dynamics of large silicic systems from satellite remote sensing observations: the intriguing case of Domuyo volcano, Argentina. Sci. Rep. 10, 11642. https://doi.org/10.1038/s41598-020-67982-8.
Lyakhovsky, V., Hurwitz, S., Navon, O., 1996. Bubble growth in rhyolitic melts: experimental and numerical investigation. Bull. Volcanol. 58, 19–32. https://doi.org/10.1007/s004450050122.
Malfait, W.J., Seifert, R., Petitgirard, S., Perrillat, J.-P., Mezouar, M., Ota, T., Nakamura, E., Lerch, P., Sanchez-Valle, C., 2014. Supervolcano eruptions driven by melt buoyancy in large silicic magma chambers. Nat. Geosci. 7, 122–125. https://doi.org/10.1038/ngeo2042.

Marianelli, P., Sbrana, A., Proto, M., 2006. Magma chamber of the Campi Flegrei supervolcano at the time of eruption of the Campanian Ignimbrite. Geology 34, 937–940. https://doi.org/10.1130/G22807A.1.
Menand, T., 2008. The mechanics and dynamics of sills in layered elastic rocks and their implications for the growth of laccoliths and other igneous complexes. Earth Planet. Sci. Lett. 267, 93–99.
Menand, T., 2011. Physical controls and depth of emplacement of igneous bodies: a review. Tectonophysics 500, 11–19.
Menand, T., Annen, C., de Saint Blanquat, M., 2015. Rates of magma transfer in the crust: Insights into magma reservoir recharge and pluton growth. Geology 43, 199–202. https://doi.org/10.1130/g36224.1.
Michel, J., Baumgartner, L.P., Putlitz, B., Schaltegger, U., Ovtcharova, M., 2008. Incremental growth of the Patagonian Torres del Paine laccolith over 90 k.y. Geology 36, 459–462 doi:10:1130/G25546A.1.
Mittal, T., Richards, M.A., 2019. Volatile degassing from magma chambers as a control on volcanic eruptions. J. Geophys. Res. Solid Earth 124, 7869–7901. https://doi.org/10.1029/2018JB016983.
Morey, G.W., 1922. The development of pressure in magmas as a result of crystallization. J. Wash. Acad. Sci. 12, 219–230.
Morgan, S., Stanik, A., Horsman, E., Tikoff, B., de Saint Blanquat, M., Habert, G., 2008. Emplacement of multiple magma sheets and wall rock deformation: Trachyte Mesa intrusion, Henry Mountains, Utah. J. Struct. Geol. 30, 491–512. https://doi.org/10.1016/j.jsg.2008.01.005.
Oppenheimer, J., Rust, A.C., Cashman, K.V., Sandnes, B., 2015. Gas migration regimes and outgassing in particle-rich suspensions. Front. Phys. 3 https://doi.org/10.3389/fphy.2015.00060.
Palummo, F., Mollo, S., Petrone, C.M., Ellis, B.S., De Astis, G., Nazzari, M., Scarlato, P., Bachmann, O., 2021. Decoding multiple zoning patterns in clinopyroxene phenocrysts at Vulcano Island: a record of dynamic crystallization through interconnected reservoirs. Lithos 406–407, 106517. https://doi.org/10.1016/j.lithos.2021.106517.
Parmigiani, A., Huber, C., Bachmann, O., 2014. Mush microphysics and the reactivation of crystal-rich magma reservoirs. J. Geophys. Res. 119.
Parmigiani, A., Degruyter, W., Leclaire, S., Huber, C., Bachmann, O., 2017. The mechanics of shallow magma reservoir outgassing. Geochem. Geophys. Geosyst. 18, 2887–2905. https://doi.org/10.1002/2017GC006912.
Peltier, A., Villeneuve, N., Ferrazzini, V., Testud, S., Hassen Ali, T., Boissier, P., Catherine, P., 2018. Changes in the long-term geophysical eruptive precursors at Piton de la Fournaise: implications for the response management. Front. Earth Sci. 6.
Petford, N., Kerr, R.C., Lister, J.R., 1993. Dike transport of granitoid magmas. Geology 21, 845–848.
Pinel, V., Jaupart, C., 2003. Magma chamber behavior beneath a volcanic edifice. J. Geophys. Res. Solid Earth 108.
Pinel, V., Jaupart, C., 2005. Some consequences of volcanic edifice destruction for eruption conditions. J. Volcanol. Geotherm. Res. 145, 68–80.
Pistone, M., Caricchi, L., Ulmer, P., Burlini, L., Ardia, P., Reusser, E., Marone, F., Arbaret, L., 2012. Deformation experiments of bubble- and crystal-bearing magmas: Rheological and microstructural analysis. J. Geophys. Res. 117.
Pistone, M., Cordonnier, B., Caricchi, L., Ulmer, P., Marone, F., 2015. The viscous to brittle transition in crystal-and bubble-bearing magmas. Front. Earth Sci. 3, 71.
Poland, M.P., Anderson, K.R., 2020. Partly cloudy with a chance of lava flows: forecasting volcanic eruptions in the twenty-first century. J. Geophys. Res. Solid Earth 125. https://doi.org/10.1029/2018JB016974.
Pollard, D.D., Johnson, A.M., 1973. Mechanics of growth of some laccolithic intrusions in Henry Mountain, Utah. 2. Bending and failure of overburden layers and sill formation. Tectonophysics 18, 311–354.
Qin, Z., Suckale, J., 2017. Direct numerical simulations of gas–solid–liquid interactions in dilute fluids. Int. J. Multiphase Flow 96, 34–47. https://doi.org/10.1016/j.ijmultiphaseflow.2017.07.008.
Reath, K., Pritchard, M., Poland, M., Delgado, F., Carn, S., Coppola, D., Andrews, B., Ebmeier, S.K., Rumpf, E., Henderson, S., Baker, S., Lundgren, P., Wright, R., Biggs, J., Lopez, T., Wauthier, C., Moruzzi, S., Alcott, A., Wessels, R., Griswold, J., Ogburn, S., Loughlin, S., Meyer, F., Vaughan, G., Bagnardi, M., 2019. Thermal, deformation, and degassing remote sensing time series (CE 2000–2017) at the 47 most active volcanoes in Latin America: implications for volcanic systems. J. Geophys. Res. Solid Earth 124, 195–218. https://doi.org/10.1029/2018JB016199.
Reath, K., Pritchard, M., Biggs, J., Andrews, B., Ebmeier, S.K., Bagnardi, M., Girona, T., Lundgren, P., Lopez, T., Poland, M., 2020. Using conceptual models to relate multiparameter satellite data to subsurface volcanic processes in Latin America. Geochem. Geophys. Geosyst. 21 https://doi.org/10.1029/2019GC008494.
Rhodes, E.L., Barker, A.K., Burchardt, S., Hieronymus, C.F., Rousku, S.N., McGarvie, D. W., Mattsson, T., Schmiedel, T., Ronchin, E., Witcher, T., 2021. Rapid assembly and eruption of a shallow silicic magma reservoir, Reyðarártindur Pluton, southeast Iceland. https://doi.org/10.1029/2021GC009999.
Rivalta, E., 2010. Evidence that coupling to magma chambers controls the volume history and velocity of laterally propagating intrusions. J. Geophys. Res. Solid Earth 115. https://doi.org/10.1029/2009JB006922.
Rubin, A.M., 1995. Getting Granite Dikes out of the Source Region. J. Geophys. Res. Solid Earth 100, 5911–5929.
Salisbury, M.J., Bohrson, W.A., Clynne, M.A., Ramos, F.C., Hoskin, P., 2008. Multiple plagioclase crystal populations identified by crystal size distribution and in situ chemical data: implications for timescales of magma chamber processes associated with the 1915 eruption of Lassen Peak, CA. J. Petrol. 49, 1755–1780. https://doi.org/10.1093/petrology/egn045.
Samaniego, P., Le Pennec, J.-L., Robin, C., Hidalgo, S., 2011. Petrological analysis of the pre-eruptive magmatic process prior to the 2006 explosive eruptions at Tungurahua volcano (Ecuador). J. Volcanol. Geotherm. Res. 199, 69–84. https://doi.org/10.1016/j.jvolgeores.2010.10.010.
Segall, P., 2013. Volcano deformation and eruption forecasting. Geol. Soc. Lond., Spec. Publ. 380, 85–106. https://doi.org/10.1144/SP380.4.
Segall, P., 2016. Repressurization following eruption from a magma chamber with a viscoelastic aureole. J. Geophys. Res. Solid Earth 121, 8501–8522. https://doi.org/10.1002/2016JB013597.
Sigmundsson, F., Pinel, V., Grapenthin, R., Hooper, A., Halldórsson, S.A., Einarsson, P., Ófeigsson, B.G., Heimisson, E.R., Jónsdóttir, K., Gudmundsson, M.T., Vogfjörd, K., Parks, M., Li, S., Drouin, V., Geirsson, H., Dumont, S., Fridriksdottir, H.M., Gudmundsson, G.B., Wright, T.J., Yamasaki, T., 2020. Unexpected large eruptions from buoyant magma bodies within viscoelastic crust. Nat. Commun. 11, 2403. https://doi.org/10.1038/s41467-020-16054-6.
Sneddon, I.N., Mott, N.F., 1946. The distribution of stress in the neighbourhood of a crack in an elastic solid. Proc. Royal Soc. London. Series A. Math. Phys. Sci. 187, 229–260. https://doi.org/10.1098/rspa.1946.0077.
Sobolev, A.V., Chaussidon, M., 1996. H2O concentrations in primary melts from supra-subduction zones and mid-ocean ridges: Implications for H2O storage and recycling in the mantle. Earth Planet. Sci. Lett. 137, 45–55. https://doi.org/10.1016/0012-821X(95)00203-O.
Spacapan, J.B., Galland, O., Leanza, H.A., Planke, S., 2017. Igneous sill and finger emplacement mechanism in shale-dominated formations: a field study at Cuesta del Chihuido, Neuquén Basin, Argentina. J. Geol. Soc. 174, 422–433. https://doi.org/10.1144/jgs2016-056.
Sparks, R.S.J., Sigurdsson, H., Wilson, L., 1977. Magma mixing: a mechanism for triggering acid explosive eruptions. Nature 267, 315–318.
Sparks, R.S.J., Annen, C., Blundy, J.D., Cashman, K.V., Rust, A.C., Jackson, M.D., 2019. Formation and dynamics of magma reservoirs. Philos. Trans. R. Soc. A Math. Phys. Eng. Sci. 377, 20180019. https://doi.org/10.1098/rsta.2018.0019.
Stock, M.J., Humphreys, M.C.S., Smith, V.C., Isaia, R., Pyle, D.M., 2016. Late-stage volatile saturation as a potential trigger for explosive volcanic eruptions. Nat. Geosci. 9, 249–254. https://doi.org/10.1038/ngeo2639.
Suckale, J., Elkins-Tanton, L.T., Sethian, J.A., 2012. Crystals stirred up: 2. Numerical insights into the formation of the earliest crust on the Moon. J. Geophys. Res. Planets 117. https://doi.org/10.1029/2012JE004067.
Suckale, J., Keller, T., Cashman, K.V., Persson, P.-O., 2016. Flow-to-fracture transition in a volcanic mush plug may govern normal eruptions at Stromboli. Geophys. Res. Lett. 43 https://doi.org/10.1002/2016GL071501, 12,071-12,081.
Tait, S., Jaupart, C., Vergniolle, S., 1989. Pressure, gas content and eruption periodicity of a shallow, crystallising magma chamber. Earth Planet. Sci. Lett. 92, 107–123. https://doi.org/10.1016/0012-821X(89)90025-3.
Tommasini, S., Bindi, L., Savia, L., Mangler, M.F., Orlando, A., Petrone, C.M., 2022. Critical assessment of pressure estimates in volcanic plumbing systems: the case study of Popocatépetl volcano, Mexico. Lithos 408–409, 106540. https://doi.org/10.1016/j.lithos.2021.106540.
Townsend, M., 2022. Linking surface deformation to thermal and mechanical magma chamber processes. Earth Planet. Sci. Lett. 577, 117272 https://doi.org/10.1016/j.epsl.2021.117272.
Townsend, M., Huber, C., Degruyter, W., Bachmann, O., 2019. Magma Chamber Growth During Intercaldera Periods: Insights From Thermo-Mechanical Modeling With Applications to Laguna del Maule, Campi Flegrei, Santorini, and Aso. Geochem. Geophys. Geosystems. 20, 1574–1591. https://doi.org/10.1029/2018GC008103.
Tramontano, S., Gualda, G.A.R., Ghiorso, M.S., 2017. Internal triggering of volcanic eruptions: tracking overpressure regimes for giant magma bodies. Earth Planet. Sci. Lett. 472, 142–151. https://doi.org/10.1016/j.epsl.2017.05.014.
Traversa, P., Pinel, V., Grasso, J.R., 2010. A constant influx model for dike propagation: Implications for magma reservoir dynamics. J. Geophys. Res. 115, B01201. https://doi.org/10.1029/2009JB006559.
van Zalinge, M.E., Mark, D.F., Sparks, R.S.J., Tremblay, M.M., Keller, C.B., Cooper, F.J., Rust, A., 2022. Timescales for pluton growth, magma-chamber formation and super-eruptions. Nature 608, 87–92. https://doi.org/10.1038/s41586-022-04921-9.
Vandemeulebrouck, J., Sabroux, J.-C., Halbwachs, M., Surono, Poussielgue, N., Grangeon, J., Tabbagh, J., 2000. Hydroacoustic noise precursors of the 1990 eruption of Kelut Volcano, Indonesia. J. Volcanol. Geotherm. Res. 97, 443–456. https://doi.org/10.1016/S0377-0273(99)00176-6.
Wallace, P.J., Gerlach, T.M., 1994. Magmatic Vapor Source for Sulfur Dioxide Released during Volcanic Eruptions: evidence from Mount Pinatubo. Science 265, 497. https://doi.org/10.1126/science.265.5171.497.
Wallace, P.J., Anderson, A.T., Davis, A.M., 1995. Quantification of pre-eruptive exsolved gas contents in silicic magmas. Nature 377, 612–616. https://doi.org/10.1038/377612a0.
Weinberg, R.F., Regenauer-Lieb, K., 2010. Ductile fractures and magma migration from source. Geology 38, 363–366. https://doi.org/10.1130/G30482.1.
White, R.A., McCausland, W.A., 2019. A process-based model of pre-eruption seismicity patterns and its use for eruption forecasting at dormant stratovolcanoes. J. Volcanol. Geothermal Res. Lessons Learn. Recent Erupt. Sinabung Kelud Volcanoes, Indonesia 382, 267–297. https://doi.org/10.1016/j.jvolgeores.2019.03.004.
Zimmerman, R.W., 2018. The imperial college lectures in petroleum engineering. In: Fluid Flow in Porous Media, Vol. 5. World Scientific (Europe). https://doi.org/10.1142/q0146.